Teleseismic attenuation, temperature, and melt of the upper mantle in the Alaska subduction zone

Roque A. Soto Castaneda[1], Geoffrey A. Abers[1], Zachary C Eilon[2], and D H Christensen[3]

[1]Cornell University
[2]University of California Santa Barbara
[3]University of Alaska Fairbanks

November 24, 2022

Abstract

Seismic deployments in the Alaska subduction zone provide dense sampling of the seismic wavefield that constrains thermal structure and subduction geometry. We measure P and S attenuation from pairwise amplitude and phase spectral ratios for teleseismic body waves at 206 stations from regional and short-term arrays. Parallel teleseismic travel-time measurements provide information on seismic velocities at the same scale. These data show consistently low attenuation over the forearc of subduction systems and high attenuation over the arc and backarc, similar to local-earthquake attenuation studies but at 10´ lower frequencies. The pattern is seen both across the area of normal Pacific subduction in the Cook Inlet, and across the Wrangell Volcanic Field where subduction has been debated. These observations confirm subduction-dominated thermal regime beneath the latter. Travel times show evidence for subducting lithosphere much deeper than seismicity, while attenuation measurements appear mostly reflective of mantle temperature less than 150 km deep, depths where the mantle is closest to its solidus and where subduction-related melting may take place. Travel times show strong delays over thick sedimentary basins. Attenuation signals show no evidence of absorption by basins, although some basins show signals anomalously rich in high-frequency energy, with consequent negative apparent attenuation. Outside of basins, these data are consistent with mantle attenuation in the upper 220 km that is quantitatively similar to observations from surface waves and local-earthquake body waves. Differences between P and S attenuation suggest primarily shear-modulus relaxation. Overall the attenuation measurements show consistent, coherent subduction-related structure, complementary to travel times.

Teleseismic attenuation, temperature, and melt of the upper mantle in the Alaska subduction zone

Soto Castaneda, R.A.[1], G.A. Abers[1], Z. Eilon[2], and D. H. Christensen[3]

[1]Department of Earth and Atmospheric Sciences, Cornell University, Ithaca NY

[2]Department of Earth Science, University of California, Santa Barbara

[3]Geophysical Institute, University of Alaska Fairbanks

Corresponding author: Geoff Abers (abers@cornell.edu) ORCID: 0000-0003-0704-2097

Key Points:

- Subducting plates and subarc-backarc mantle are clear from body-wave attenuation measurements
- The Wrangell Volcanic Field is underlain by Yakutat subduction, but geometry is complex
- Sedimentary basins unexpectedly produce negative apparent attenuation in body-wave spectra.

Abstract

Seismic deployments in the Alaska subduction zone provide dense sampling of the seismic wavefield that constrains thermal structure and subduction geometry. We measure *P* and *S* wave attenuation from pairwise amplitude and phase spectral ratios for teleseismic body waves recorded at 206 stations from regional and short-term arrays. Parallel teleseismic travel-time measurements provide information on seismic velocities at the same scale. These data show consistently low attenuation over the forearc of subduction systems and high attenuation over the arc and backarc, similar to local-earthquake attenuation studies but at 10× lower frequencies. The pattern is seen both across the area of normal Pacific subduction in the Cook Inlet, and across the Wrangell Volcanic Field where subduction has been debated. These observations confirm subduction-dominated thermal regime beneath the latter. Travel times show evidence for subducting lithosphere much deeper than seismicity, while attenuation measurements appear mostly reflective of mantle temperature less than 150 km deep, depths where the mantle is closest to its solidus and where subduction-related melting may take place. Travel times show strong delays over thick sedimentary basins. Attenuation signals show no evidence of absorption by basins, although some basins show signals anomalously rich in high-frequency energy, with consequent negative apparent attenuation. Outside of basins, these data are consistent with mantle attenuation in the upper 220 km that is quantitatively similar to observations from surface waves and local-earthquake body waves. Differences between *P* and *S* attenuation suggest primarily shear-modulus relaxation. Overall the attenuation measurements show consistent, coherent subduction-related structure, complementary to travel times.

Plain Language Summary

Seismic waves lose more energy passing through hot and partly molten parts of the earth than cold rigid regions. As a result, measurements of variation in their amplitudes, or attenuation, provides a tool for mapping out the upper mantle, complementing more traditional measurements of their variation in travel time. New high-quality arrays across southern Alaska, along with recent methodological developments, now allow this measurement to be made systematically across the entire region. They show consistently low attenuation where subducting plates are near the surface or along paths that follow the cold subducting plates. These regions are in southernmost Alaska. By contrast, signals traveling beneath volcanic regions or north of them, where hot mantle flows toward subduction zones, show high attenuation. The attenuation patterns resemble those from travel time, but seem to show more sensitivity to the upper 150 km of the Earth while travel time delays more uniformly sample deeper. Sedimentary basins show confusing signals, with travel time delays as expected for low-wavespeed sediments, but high amplitudes that are difficult to explain. These signals allow quantitative mapping of temperature and melt variations in the upper mantle, even in regions as complex as subduction zones where both properties vary rapidly over short distances.

1 Introduction

Seismic imaging offers critical insight into mantle thermal structure and melting in subduction zones. While seismic velocities provide first-order constraints, alone they suffer from ambiguities in resolving melt from temperature (e.g., Hammond & Humphreys, 2000a) and are sensitive to composition and crustal geology. Seismic attenuation (parameterized by its reciprocal, the quality factor *Q*) can provide powerful constraints with greater sensitivity to temperature, potentially to melt, and relatively less to composition than velocity measurements

(Karato 2003; Faul & Jackson, 2005; Dalton et al. 2009; Takei, 2017). In subduction zones, high attenuation (low *Q*) beneath volcanic arcs exceeds that predicted by temperature alone and likely indicates some in situ melt (Abers et al., 2014). That observation contrasts strongly with the negligible attenuation seen within subducting plates and shallow forearcs where temperatures are expected to be very low (e.g., Roth et al., 1999; Stachnik et al., 2004; Pozgay et al., 2009; Wei & Wiens, 2018). However, such observations are limited because rely upon signals from earthquakes within the Wadati-Benioff Zone (WBZ) directly beneath seismometers, so are available only directly above regions of abundant WBZ seismicity. Recent developments in the use of teleseismic waveforms, used here, avoid this limitation and provide potentially comparable resolution for teleseismic velocity and attenuation studies (Eilon & Abers, 2017).

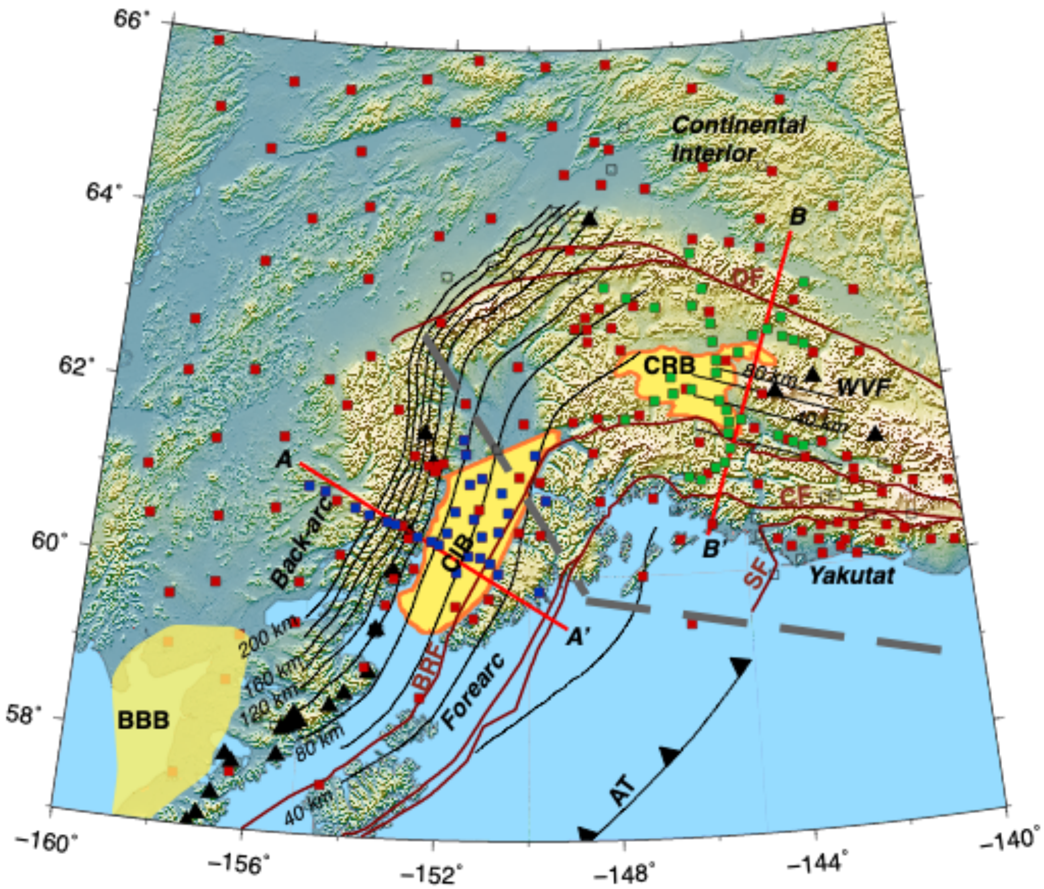

Figure 1. *Alaska study region and major features. Black lines: Wadati-Benioff zone contours at 20 km intervals; dark red lines: major terrane-bounding faults; yellow areas: Cook Inlet (CIB), Copper River (CRB) and Bristol Bay (BBB) basins; gray dashed line: inferred west edge of Yakutat terrane; black triangles: Quaternary volcanoes. Squares are seismometers examined in this study, filled if used in final results and open if not, blue are SALMON and green are WVLF short-term deployments while red are other stations. Red lines A-A' and B-B' show transects across Cook Inlet and WVF respectively. Other abbreviations: WVF, Wrangell Volcanic Field; DF, Denali Fault; CF, Contact Fault; BRF, Border Ranges Fault.*

South central Alaska provides a relatively accessible, modern example of the complexities present where subduction systems terminate along strike. The eastern, largely amagmatic, east end of the Aleutian subduction system gives way to the Wrangell Volcanic Field (WVF) just north of the Yakutat collision (e.g., Plafker & Berg, 1994). The relationship between the WVF and subduction remains controversial (e.g., Martin-Short et al., 2016; Jiang et al., 2018;

Martin-Short et al., 2018). The expansion of the EarthScope Transportable Array (TA) to south central Alaska beginning in 2014 has provided some of the first seismic imaging of the region at moderate resolution, and here we augment that dataset with observations from two focused high-resolution broadband seismic deployments, WVLF (Wrangell Volcanism and Lithospheric Fate; Christensen & Abers, 2016) and SALMON (Tape et al., 2017). We extract information about both seismic attenuation and seismic velocities from teleseismic body waves (Eilon & Abers, 2017), in an attempt to untangle the effects of composition, temperature, melt, and near-surface effects. The data show clear signatures of subduction and the hot mantle wedge beneath both the eastern Aleutian arc and the WVF.

1.1 Tectonic Setting

South-Central Alaska (**Figure 1**) was formed by a series of collisions of exotic terranes, culminating in the Cenozoic collision of the Yakutat terrane into the North American continent (Plafker & Berg 1994; Trop & Ridgway, 2007). The Yakutat terrane is likely an oceanic plateau currently converging with south-central Alaska (e.g., Bruns 1983; Christeson et al., 2010; Worthington et al., 2012). Its 15-25 km thick crust has been imaged subducting to at least 140 km depth beneath the Alaska Range west of 147°W, where intermediate-depth seismicity is abundant (Ferris et al., 2003; Eberhart-Phillips et al., 2006). To the east, its fate is more ambiguous; at shallow depths the Yakutat block actively underthrusts coastal Alaska (Pavlis et al., 2004; Elliott & Freymueller, 2020), but it is unclear whether Yakutat lithosphere subducts coherently or collides. The Yakutat basin overlies the Yakutat terrane and comprises various Cenozoic sedimentary strata reaching 10 km in thickness (Trop & Ridgway 2007).

The subduction of the Pacific Plate beneath the 3000 km long Aleutian island arc causes extensive arc volcanism as far east as Cook Inlet (Buurman et al., 2014). Although Wadati-Benioff zone (WBZ) seismicity continues another 350 km farther east, volcanism is absent with the exception of a small Quaternary maar roughly overlying the east end of intermediate-depth seismicity (Plafker & Berg, 1994; Nye et al., 2018). The WVF contains several active volcanoes younger than 25 Ma (Richter et al., 1990) with generally calc-alkaline, arc-like eruptive products, with some exceptions (Preece & Hart, 2004); the presence of adakitic ashes and lavas potentially indicates slab-edge-type melting (Brueske et al., 2019). Some recent tomographic analyses of seismic surface and body waves wave tomography indicate a high velocity anomaly extending 85-100 km past the edge of the WBZ at 147°W (Wang & Tape, 2014; Ward, 2015; Jiang et al., 2018), although other studies do not (Martin-Short et al., 2018; Berg et al., 2020). The same studies also disagree over the extent and existence of the slab beneath the WVF.

2. Data

We examine data from broadband seismometers between 55˚ and 65˚ N and 160˚ to 140˚ W collected between 2015 and 2017 from both portable and long-term arrays in the region (**Figure 1**). Data come from the Earthscope Transportable Array and permanent regional networks (Ruppert & West, 2019) as well as two dense short-term arrays, WVLF and SALMON. The WVLF array featured 35 broadband seismometers deployed from June 2016 to June 2018 in the Central Alaska subduction zone and WVF regions (McPherson et al., 2020); this study only analyzes the first year of recording. The SALMON array includes 28 broadband, direct-burial posthole seismometers spanning the Cook Inlet region of the Alaska Subduction zone from summer 2015 to summer 2017 (Tape et al., 2017).

The primary signals are teleseismic (30°-90° distance) *P* and *S* waveforms, measured on vertical and transverse components, respectively, These signals are suitable for both cross-correlation for travel times and frequency-dependent analysis for attenuation as described below. Usable data were obtained for 167 teleseisms with $M_W \geq 6.0$ from June 2015 through July 2017, recorded across 206 unique stations. Three-component seismic waveforms were down-sampled to 10 samples per second to achieve a parity in the sampling rate for data from different arrays, and the instrument response was removed. Waveforms were windowed 40 s before and after the predicted arrival and then extended 20% prior to applying a 20% Tukey window.

Core-phase interference (*SKS*) can complicate *S* waves, so we tested a maximum epicentral distance cutoff of 70º for *S*. The cutoff diminished the pool of available events from 167 to 32 and resulted in poor azimuthal coverage, but showed no systematic changes to results, so our final analysis used events from the full 30˚-90˚ range. Our use of the transverse component isolates the SH component of the *S* waves, minimizing the impact of *SKS* energy within this window as well as other P-S mode-converted signals, which are to first order radially polarized. Notwithstanding, signals that have visible overlap of *SKS* and *S* within the spectral calculation window (described below) on more than half of the recorded traces are manually discarded. After this and other quality control described below, 89 earthquakes were used for both *S* and *P* phases.

3. Methods

The primary measurements were differential travel times (ΔT) and differential integrated attenuation values (Δt^*) for each usable station – event pair. The methods and workflow are described elsewhere (Eilon & Abers, 2017; Soto Castaneda, 2020) and summarized here. The station-specific ΔT and Δt^* were derived from differential measurements between each pair of stations for every event. Different subsets of events were recorded by each individual station, and each individual event was recorded at different subsets of stations. We therefore jointly inverted all pairwise data as described below, treating velocity or attenuation from *P* or *S* signals as four separate inversions, to solve for event terms and single values of ΔT or Δt^* for each station.

3.1. Differential Travel Times

To calculate the ΔT, waveforms were cross-correlated after applying a bandpass filter of 0.083 – 1 Hz and from 0.2 – 1 Hz for the *S* and *P* waveforms respectively, within a hand-picked window of 10 – 20 s duration around the first arrival. We discarded waveform pairs with cross-correlation coefficients of less than 0.65. The remaining traces were used to compute single-station travel time residuals, ΔT, following standard methods (VanDecar & Crosson, 1990). These frequency-independent station residuals were then applied to align waveforms for attenuation measurements. This procedure resulted in 8061 ΔT_P and 7565 ΔT_S measurements.

3.2 Attenuation

Differential attenuation Δt^* was derived from spectral ratios of station pairs. After deconvolving instrument response, the differences in signal between stations are attributed to differential attenuation between paths to the two stations. These measurements are described by a differential attenuation operator

$$\Delta t_{ij}^* = \Delta t_i^* - \Delta t_j^* \quad (1)$$

as the difference between Δt^* recorded at station i and j (e.g., Roth et al., 1999). In amplitude and phase the spectral ratios are related to this operator as:

$$\ln\left(R_{ij}(f)\right) = k_{1ij} - \pi f \Delta t^*{}_{ij}, \tag{2}$$

$$\Delta\varphi_{ij}(f) = k_{2ij} + \frac{1}{\pi}\ln\left(\frac{f}{f_0}\right)\Delta t^*{}_{ij}, \tag{3}$$

where $R_{ij}(f)$ is the spectral amplitude ratio between stations i and j, $\Delta\varphi_{ij}(f)$ is the spectral phase shift, k_{1ij} describes a frequency-independent differential amplification between stations, k_{2ij} represents a frequency-independent phase shifts (Eilon & Abers, 2017), and f_0 is the reference frequency (chosen to be 1 Hz). Each pairwise measurement of amplitude ratio R_{ij} and differential phase $\Delta\varphi_{ij}$ over a range of frequency f provides a constraint on the corresponding differential attenuation operator Δt^*_{ij}.

We test for frequency dependence of attenuation of the form $t^*(f) = t^*_0 f^{-\alpha}$ typical of many descriptions and laboratory measurements (e.g., Faul & Jackson, 2005), where t^*_0 is the integrated attenuation at the reference frequency. The expressions in equations 2 and 3 are appropriate for frequency independent ($\alpha = 0$) attenuation (e.g., Faul & Jackson, 2005; Stachnik et al., 2004). Following several studies that show weak frequency dependence of $\alpha = 0.27$, we also test this case, leading to a modification of the expressions (e.g., Anderson & Minster, 1979; Eilon & Abers, 2017):

$$\ln\left(R_{ij}(f)\right) = k_{1ij} - \pi f_0^{\alpha} f^{1-\alpha}\Delta t^*_{0ij}, \tag{4}$$

$$\Delta\varphi_{ij}(f) = k_{2ij} + \frac{1}{2}\cot\left(\frac{\alpha\pi}{2}\right) f_0^{\alpha} f^{-\alpha}\Delta t^*_{0ij}. \tag{5}$$

3.3. Measurements of amplitude, phase and Δt^*

Amplitude ratios and phase differences between stations recording the same earthquake are measured at a range of narrow frequency bands, through a multiple-narrowband-filter technique (Dziewonski et al. 1969). This filter-bank method has been demonstrated to improve upon Fourier-domain amplitude spectral ratio methods by increasing the range of useable frequencies and through the inclusion of phase data (Bezada et al., 2019; Soto Castaneda, 2020). For a 35 s window starting 5 s before the first arrival, each trace is run through a comb of 30 narrow-band filters logarithmically spaced in center frequency from 0.05 – 0.5 Hz (Eilon, 2016). At each frequency for which the signal exceeds noise, the $\Delta\varphi_{ij}$ and R_{ij} for each station pair are measured by time-shifting and amplitude-scaling signals in the time domain from these narrow-band-filtered waveforms (e.g., **Figure 2**). The squared correlation-coefficient between shifted and scaled waveforms at each individual frequency is used to weights $w_{ij}(f)$ used in the subsequent inversion for Δt^*, ensuring that we only compare portions of the spectra for which the two waveforms are compatible. Only measurements for which correlation coefficients exceed 0.5 are retained. We discard any station pair for which fewer than four frequencies have signal that exceeds 10 times the pre-event noise, and any trace for which the cross-correlation coefficient with the stacked trace for that event is less than 0.5.

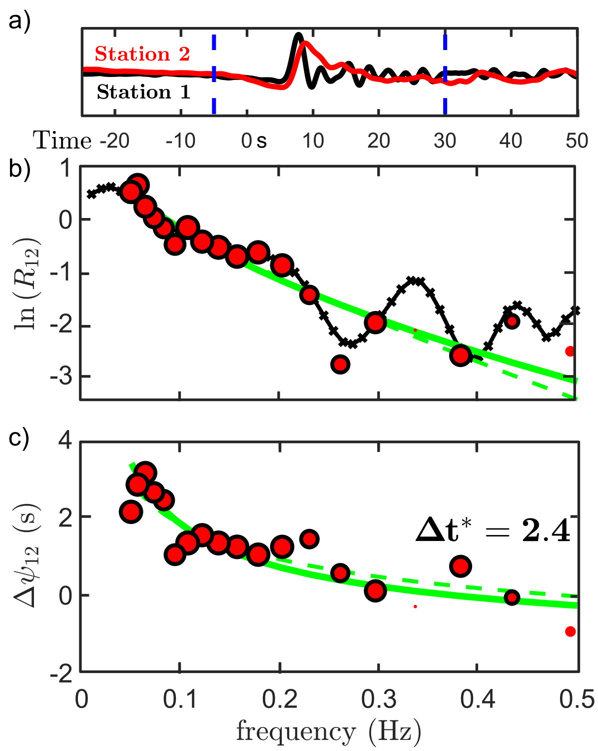

Figure 2*. (a) Example of S-wave differential attenuation measurement between two stations, CUT (Chulitna, Alaska; black) and RED (Mount Redoubt, Alaska; red). Blue lines indicate windows for spectra calculation. (b) logarithm of amplitude ratios. (c) differential phase. In (b) and (c), red circles are measurements at each narrow band filter; size reflects robustness of measurement of each narrow band as measured by maximum cross-correlation. Solid green line: best fit assuming no frequency dependence of attenuation; dashed green line best fit assuming frequency dependence coefficient of 0.27. Black line in (b) is the spectral ratio calculated by spectral division.*

For each phase, station-specific Δt_i^* values are determined by minimizing

$$E = A \sum_{ijm} w_{ijm} \left(\ln\left(R_{ijm}^{obs}\right) - \ln\left(R_{ijm}\right)\right)^2 + \sum_{ijm} w_{ijm} \left(\Delta\varphi_{ijm}^{obs} - \Delta\varphi_{ijm}\right)^2 \qquad (6)$$

combining (1) with either (2)-(3) or (4)-(5), where R_{ijm} is the predicted amplitude ratio from (2) or (4) at the m^{th} frequency, $\Delta\varphi_{ijm}$ is the corresponding phase ratio, R_{ijm}^{obs} and $\Delta\varphi_{ijm}^{obs}$ are their respective observations, w_{ijm} is as above, and A is a factor controlling the relative weighting of amplitude to phase misfit. After several trials, A is set to 2.0 in results presented here. This error function is minimized over all frequencies that meet the signal-to-noise criterion, solving for station-specific Δt_i^* via linear least-squares inversion.

After solving for individual station terms, this procedure generates 4281 Δt_P^* and 3663 Δt_S^* measurements, for 89 earthquakes. A second least-squares inversion determines best Δt_P^* and Δt_S^* estimates for each station from these single-earthquake Δt^* measurements, simultaneously determining the 206 station-specific Δt^*, earthquake source terms, and standard errors. The earthquake source terms are not discussed further, but are necessary to account for differences in the station subsets recording different earthquakes.

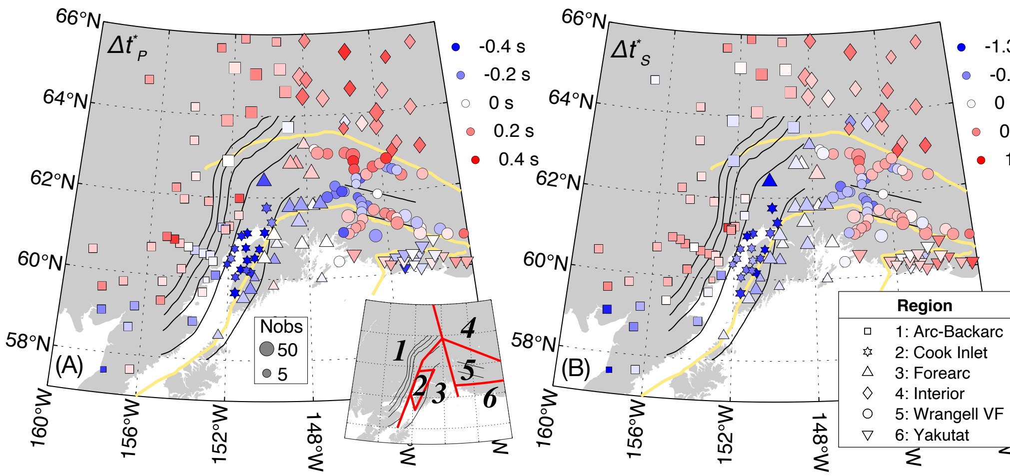

Figure 3. *Station-averaged Δt* measurements, from simultaneous inversion for station terms and event terms as described in text. The Δt* at each station determined for each earthquake assumes an amplitude/phase weight ratio of 2.0. Black lines show contours to slab surface 40 km intervals (Li et al., 2013; Daly et al., 2019). Symbols show Δt* values plotting at each station, with size scaled to square root of number of observations ("Nobs" in legend, left panel) and color by value, as indicated by legends to upper right. Symbol shapes indicate regions (inset) named and numbered as shown in legend on lower left. Black lines: WBZ depth contours at 40 km intervals; yellow lines: Denali, Border Ranges, and St Elias faults (Fig. 1).*

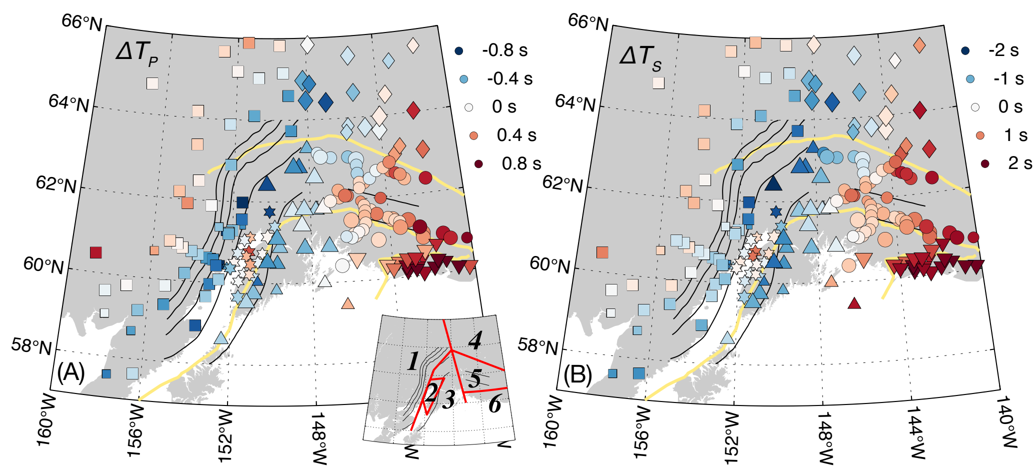

Figure 4. *Station-averaged ΔT measurements, from simultaneous inversion for station terms and event terms as described in text. Symbols as in Figure 3.*

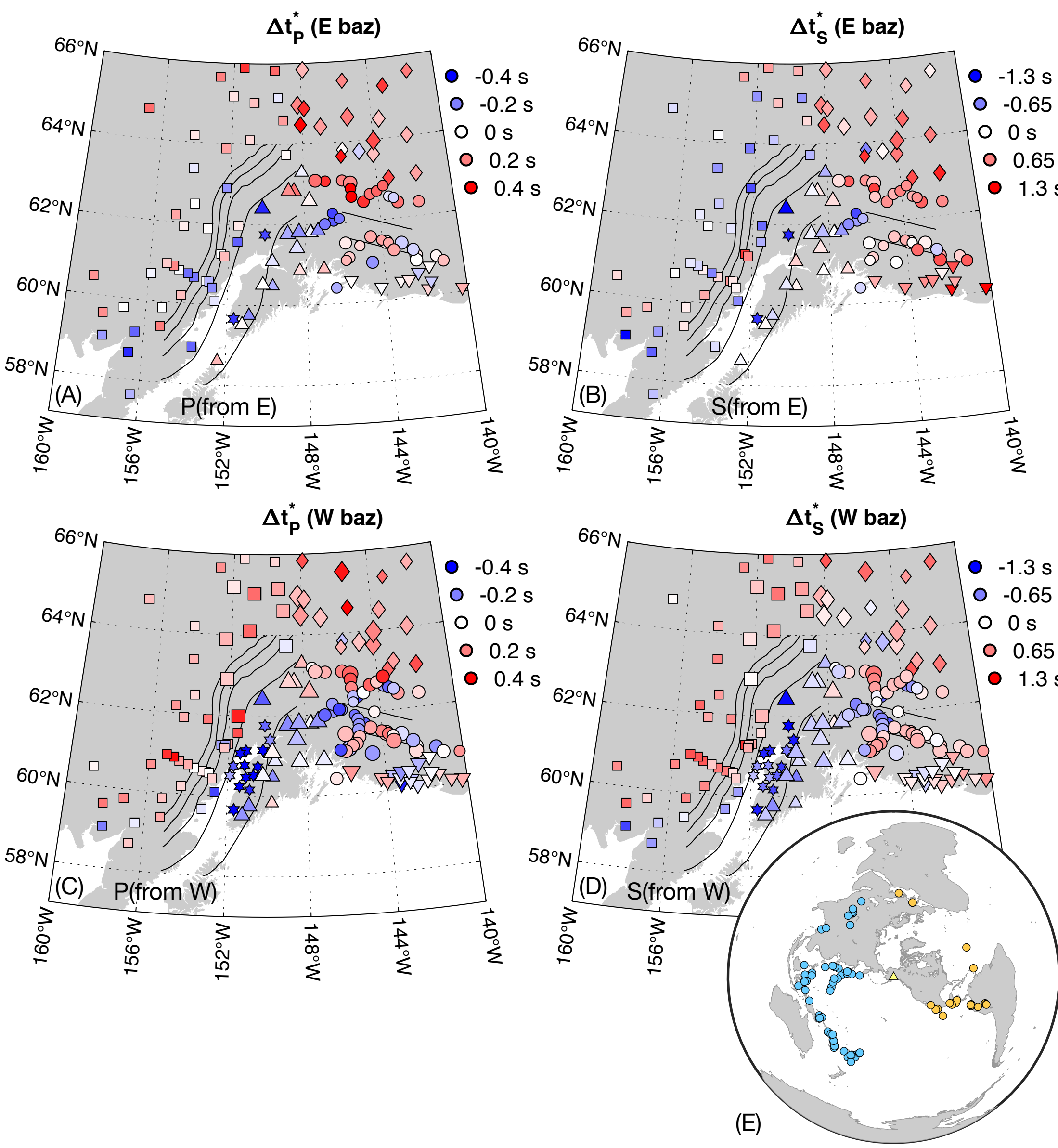

Figure 5*. Differential Δt* values per station, separated by back-azimuth. (A) P waves, back azimuths from east. (B) S waves, back azimuths from east. (C) P waves, back azimuths from west. (D) S waves, back azimuths from west. (E) Global map of earthquakes colored by back-azimuthal bin. Symbols as in Figure 3.*

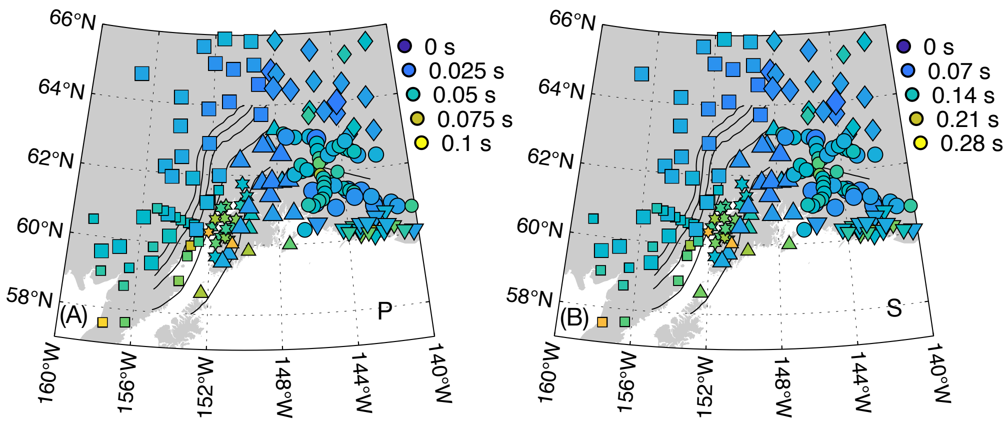

Figure 6. *Standard deviation of station-averaged Δt^* measurements, as formal errors in simultaneous inversion for station terms and event terms as described in text. The Δt^* at each station determined for each earthquake assuming an amplitude/phase weight ratio of 2.0. Symbols as in Figure 3.*

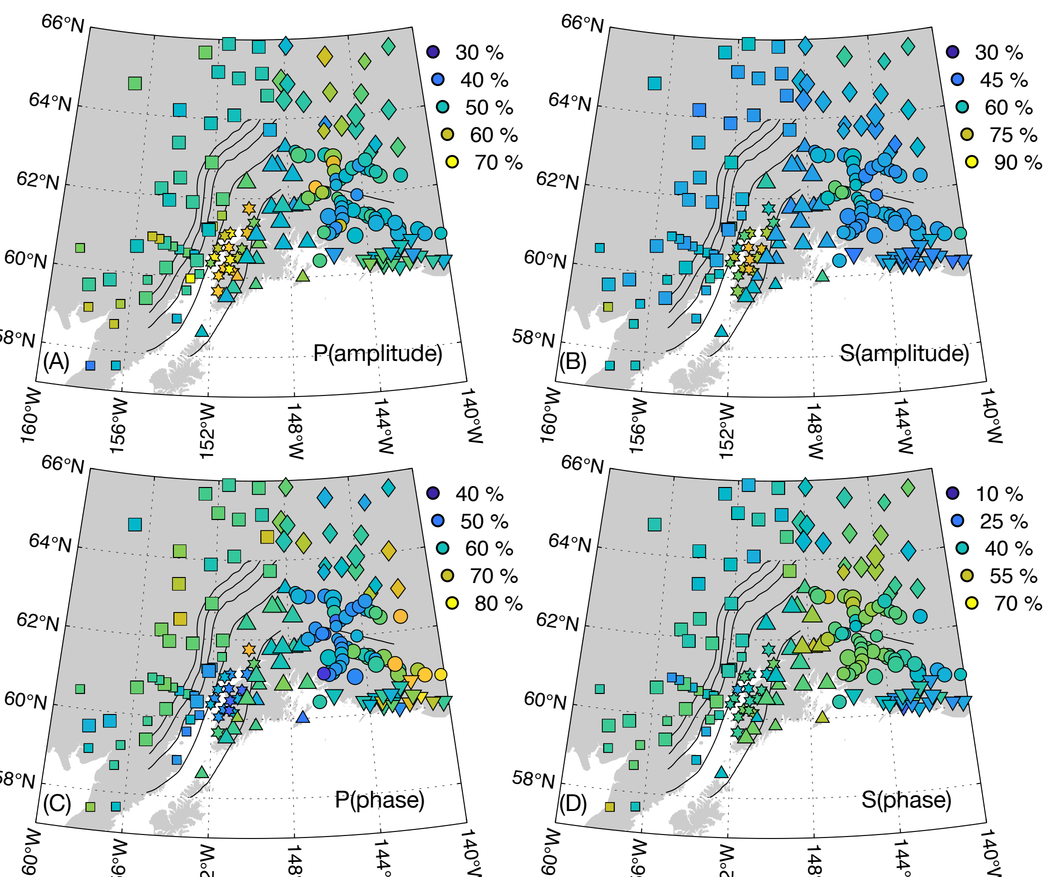

Figure 7. *Variance reduction in fitting spectra comb to station Δt^*. (A) P waves, variance of amplitude spectra fit. (B) S waves, variance of amplitude spectra fit. (C) P waves, variance of phase spectra fit. (D) S waves, variance of phase spectra fit. Colors show variance reduction relative to total variance in amplitude or phase, averaged over each station-pair spectral ratio involving the given station, and averaged over all earthquakes. Larger variance reduction indicates better fit to spectra. Δt^* at each station determined for amplitude/phase weight ratio of 2.0. Symbols as in Figure 3.*

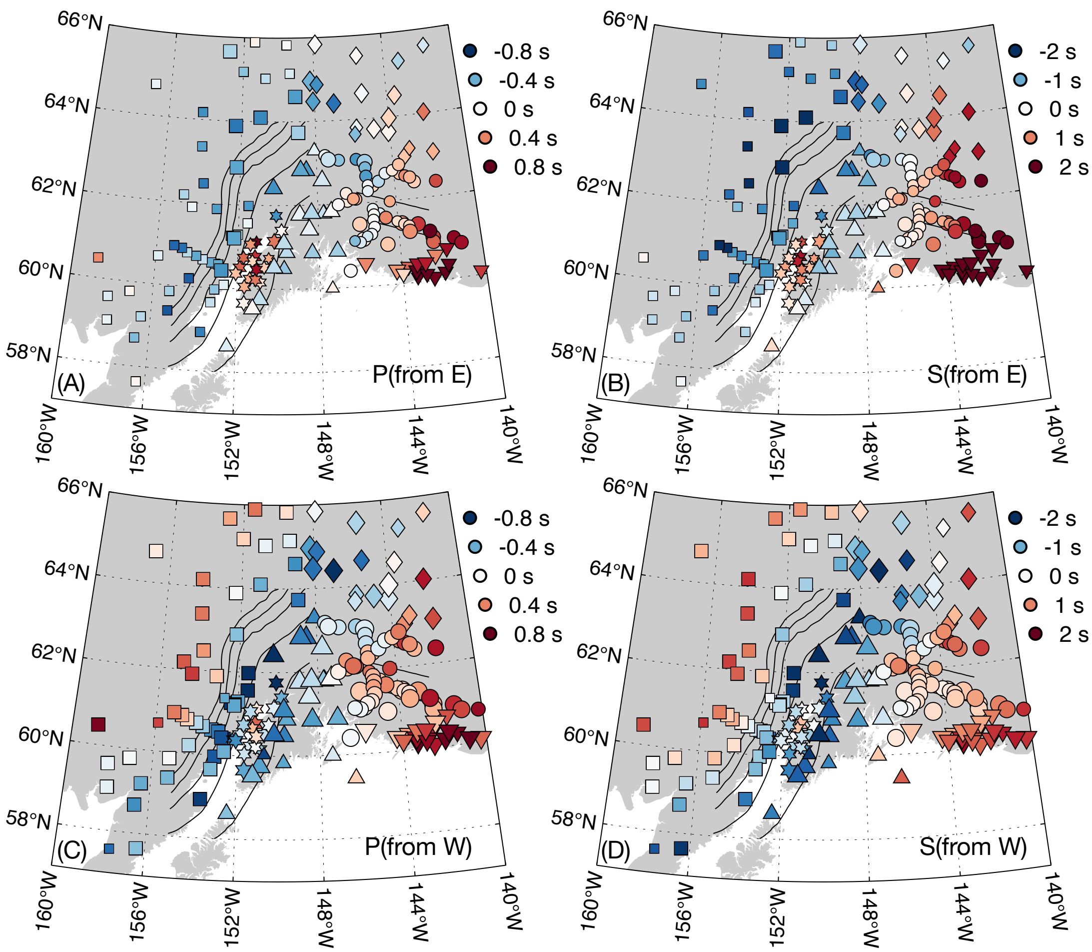

Figure 8. *Differential travel-time residual (ΔT) station averages, separated by back azimuth. (A) P waves, back azimuths from east. (B) S waves, back azimuths from east. (C) P waves, back azimuths from west. (D) S waves, back azimuths from west. Symbols as in Figure 3.*

4. Results

4.1 Overview

Station values are determined from all events (**Figures 3, 4**), or from one of two subsets of earthquakes at either western or eastern back-azimuths (**Figure 5**), along with standard errors computed from variability between measurements at a given station (**Figure 6**). The per-station ΔT estimates derive from pairwise cross-correlation lags at all stations and all earthquakes in the population. The Δt^* estimates are determined by the procedure described above. As an alternative method of evaluating uncertainty in Δt^*, we calculate the separate reductions in variance from fitting amplitude and fitting phase spectra (from the first and second sums on the right-hand side of equation 6), averaged over events weighted by number of observations (**Figure 7**). The results indicate strong spatial correlations between nearby measurements but large variations between regions, in both Δt^* and ΔT. Standard deviation estimates are generally largest in and around basins, although the variance reduction for amplitude spectra is also largest in those locations.

Some patterns are clearer after binning stations into one of six tectonic regions (**Figure 3**), defined as follows. Region 1 is the Aleutian arc-backarc, bounded in the east by the edge of the Alaskan-Aleutian WBZ and by the 75 km slab depth contour to the south. Region 2 surrounds the Cook Inlet Basin, bounded by the Border Range Fault in the south and Region 1 to the north. Region 3 is the Aleutian Forearc, bounded by the limit of Alaska-Aleutian WBZ seismicity in the east and Regions 1 or 2 to the north and west. Regions 1 – 3 comprise normal Pacific or Yakutat plate subduction, with a clear WBZ. Region 4, the Continental Interior region, lies north of the Denali fault and east of Aleutian WBZ. Region 5 is centered on the WVF and lies south of the Denali fault but north of the Contact Fault zone, east of the Aleutian WBZ. Finally, Region 6 the Yakutat region lies south of the Contact Fault, coincident with and directly surrounding exposed deformed sediments of the Yakutat terrane. Within regions 5 and 6 the ΔT, but not the Δt^*, show a broad trend toward slower arrivals moving further east in both *P* and *S*, indicating variability at a scale large compared with array aperture. **Table 1** shows mean values of Δt^* and ΔT for each region, along with standard errors for the station terms.

TABLE 1. Regional averaged ΔT and Δt^*

Region	Name	ΔT_P (s)[1]	ΔT_S (s)	Δt^*_P (s)	Δt^*_S (s)	N[2]	Nst[3]
All earthquakes							
1	Arc/backarc	-0.21 ± 0.01	-0.41 ± 0.03	0.07 ± 0.01	0.17 ± 0.01	46	53
2	Cook Inlet	-0.04 ± 0.02	-0.09 ± 0.05	-0.35 ± 0.01	-0.94 ± 0.02	17	18
3	Forearc	-0.31 ± 0.01	-0.9 ± 0.04	-0.05 ± 0.01	-0.21 ± 0.01	45	24
4	Cont. Int.	-0.12 ± 0.02	-0.14 ± 0.06	0.18 ± 0.01	0.41 ± 0.01	53	19
5	Wrangell	0.22 ± 0.01	0.64 ± 0.03	0.03 ± 0.01	0.15 ± 0.01	49	52
6	Yakutat	0.58 ± 0.02	01.67 ± 0.03	0.01 ± 0.01	0.29 ± 0.02	30	19
East back-azimuth (0-180°)							
1	Arc/backarc	-0.31 ± 0.02	-01.3 ± 0.05	0.03 ± 0.01	-0.11 ± 0.02	14	47
2	Cook Inlet	0.29 ± 0.03	0.55 ± 0.09	-0.3 ± 0.01	-01.02 ± 0.05	8	10
3	Forearc	-0.21 ± 0.02	-0.64 ± 0.06	-0.04 ± 0.01	-0.14 ± 0.03	15	20
4	Cont. Int.	-0.07 ± 0.04	0.08 ± 0.14	0.19 ± 0.01	0.52 ± 0.03	18	19
5	Wrangell	0.17 ± 0.03	0.91 ± 0.08	0.06 ± 0.01	0.22 ± 0.02	18	48
6	Yakutat	0.63 ± 0.04	02.56 ± 0.08	0.03 ± 0.01	0.70 ± 0.05	8	12
West back-azimuth (180-360°)							
1	Arc/backarc	-0.19 ± 0.02	-0.19 ± 0.05	0.1 ± 0.01	0.34 ± 0.02	32	50
2	Cook Inlet	-0.18 ± 0.03	-0.60 ± 0.07	-0.39 ± 0.01	-0.9 ± 0.03	10	16
3	Forearc	-0.37 ± 0.02	-01.19 ± 0.05	-0.05 ± 0.01	-0.26 ± 0.02	30	21
4	Cont. Int.	-0.17 ± 0.03	-0.40 ± 0.08	0.18 ± 0.01	0.33 ± 0.02	35	19
5	Wrangell	0.22 ± 0.01	0.35 ± 0.03	0.01 ± 0.01	0.10 ± 0.01	31	52
6	Yakutat	0.53 ± 0.02	01.16 ± 0.03	0.00 ± 0.01	0.13 ± 0.02	23	18

(1) uncertainties are 2-sigma standard errors from joint station- and event-term inversions
(2) number of earthquakes used in each estimate
(3) number of stations recording at least 4 earthquakes in each subset

4.2. Regions 1 & 3 - Alaska-Aleutian Subduction

The Alaska-Aleutian subduction region has a typical geometry of subduction, showing a clear WBZ to >150 km depth and a high-velocity and high-*Q* subducting lithosphere (Page et al., 1989; Ratchkovski & Hansen 2002; Eberhart-Phillips et al., 2006; Martin-Short et al., 2018; Nayak et al., 2020). The ΔT results confirm this pattern, showing some of the fastest raypaths (most negative residuals) over the shallower part of the subducting plate and slow paths in the backarc (**Figures 4, 8**). For example, ΔT_S in the backarc (Region 1) is on average 0.49 s slower (larger) than the forearc (Region 3), with that difference reaching 1.0 s for the west back-azimuthal subset (**Table 1, Figure 8d**) that is maximally sensitive to the slab structure.

The Δt^{*} measurements (**Figures 3, 5**) show a clear difference between high attenuation in Region 1, and low attenuation in Region 3. The arc-backarc (Region 1) shows on average 0.38 s larger Δt_S^* than the forearc (Region 3). In detail, the implied gradient in attenuation arises from slab structure: there is no significant difference in Δt_S^* between these two regions for teleseisms incident from the east that barely sample the mantle wedge (**Figure 5**). By contrast, western back-azimuth paths average 0.60 s of Δt_S^* difference between these regions, and for single stations, differences can reach 2.5 s. Raypaths from the west (chiefly from earthquakes in western Pacific subduction zones; **Figure 5e**) are nearly parallel to the slab, so forearc stations record rays that spend considerable time in the cold subducting lithosphere while raypaths to back-arc stations almost entirely sample the hot mantle wedge.

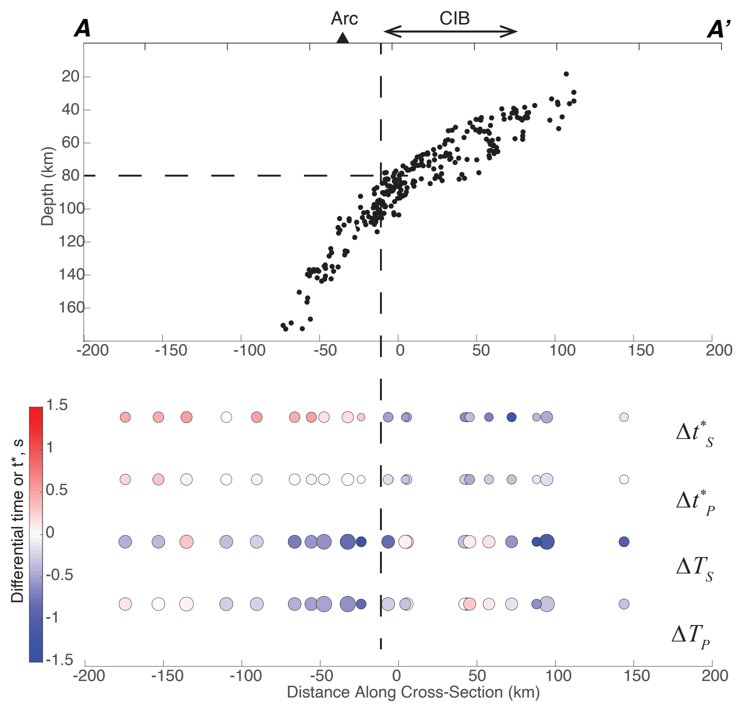

Figure 9. *Cross section of results and seismicity through Cook Inlet; A-A' from Figure 1. Top: local seismicity from AEC catalog, 2016-2018 for earthquakes within 25 km of cross section, with depth errors < 1 km. Triangles: volcanic arc. CIB: Cook Inlet Basin. Bottom: station averages of differential travel time or attenuation operator as labeled, for all stations within 50 km of the cross section on Figure 1. Dashed line shows transition from high to low attenuation. Symbol size as in Figure 3.*

These results resemble those of local attenuation studies along the Denali segment transect (Stachnik et al. 2004), and a preliminary examination of the Cook Inlet segment beneath the SALMON array (Mann & Abers, 2020). Stations located above slab depths of 80 km or greater (Region 1) not only show higher attenuation (especially for the S phase) than those in the forearc, but also show delayed arrivals and an increase in attenuation farther into the backarc. In cross section (**Figure 9**) there is a clear break between negative and positive Δt_S^* (and to somewhat less extent Δt_P^*) where the top of the WBZ is ~80 km deep, consistent with mantle-wedge attenuation structure of subduction zones worldwide (Abers et al., 2014; 2017; 2020). Thus, it seems likely that the teleseismic attenuation signal is dominated by the same depth range (upper 100-150 km) as dominates local earthquake attenuation. By contrast, ΔT shows negative (fast) residuals much farther downdip. Either attenuation anomalies are limited to a more restricted depth range than travel time anomalies, or teleseismic Δt^* measurements have a more limited depth sensitivity to Q than do ΔT measurements to V. A slow anomaly at +0 to +60 km along this section sits over the Cook Inlet Basin is likely a basin effect, discussed below.

4.3. Region 4 - The Continental Interior

The Continental Interior region shows generally high attenuation with the highest positive mean Δt_P^* and Δt_S^* of any region (0.18 ± 0.01 s and 0.41 ± 0.01 s respectively) but no clear spatial patterns within the region. By comparison, the ΔT measurements evince a longitudinal gradient with ΔT_S increasing from less than -1.0 s at the eastern edge of the Aleutian WBZ (~149°W) to more than +1.5 s at the Canadian border (141°W). These variations in ΔT exist in both back-azimuthal subsets (**Figure 8**). Additionally, more positive (slow) arrivals from the eastern back-azimuth suggest a large, slow region somewhere east of the array. The long wavelength of this gradient, larger than the array, and comparison with tomography suggests a deep source relative to the width of the array, perhaps near the transition zone as seen in some tomography and inferred from discontinuity topography (e.g., Jiang et al., 2018; van Stiphout et al., 2019). Travel time but not Δt^*shows evidence of this deeper structure.

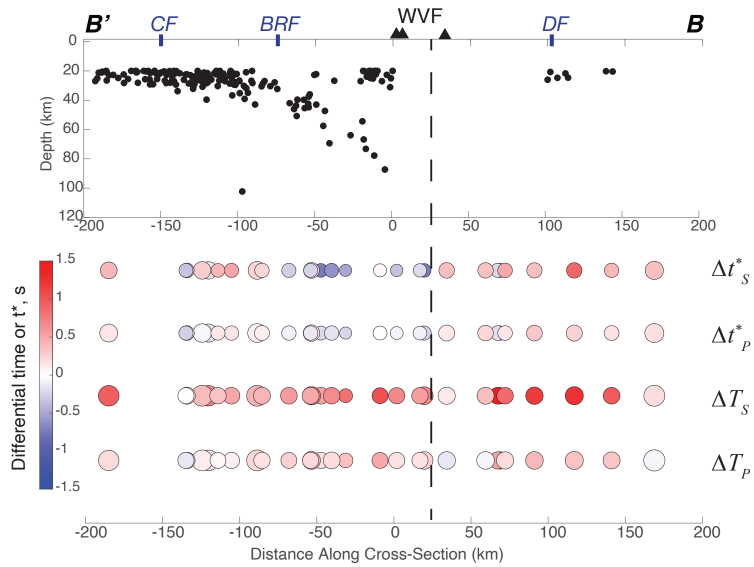

***Figure 10**. Cross section through Wrangell Volcanic Field (WVF), B-B' on Figure 1. Top: local seismicity from AEC catalog, 1999-2018 for earthquakes within 25 km of cross section, with depth errors < 1 km. Triangles: volcanic arc. Bottom: station averages of differential travel time or attenuation operator as labeled, for all stations within 50 km of the cross section, shown on Figure 1. Vertical dashed line shows transition from high to low attenuation. Symbol size as in Figure 3. Terrane bounding faults: CF, Contact Fault; BRF, Border Ranges Fault System; DF, Denali Fault.*

4.4 Region 5 - The Wrangell Volcanic Field

The Wrangell region (Region 5) shows fast arrivals to the northwest of the WVF, and slower arrivals elsewhere, dominated by slow arrivals with mean ΔT_S and ΔT_P of 0.64 ± 0.03 s and 0.22 ± 0.01 s respectively. In both *S* and *P*, arrivals become slower toward the south where thick Yakutat sediments occur (see below). The pattern differs from that of the Alaska-Aleutian subduction system which show fast paths associated with subducted lithosphere. By comparison, the Δt^* pattern across the WVF more resemble those within the Cook Inlet – Kenai region of Alaska-Aleutian subduction. There is a sharp boundary between low-attenuation regions just south of the WVF (the forearc) transitioning to high-attenuation regions further north (the hot mantle wedge) over distances as short as ~30 km (**Figure 10**). This step is at least 1.0 s in Δt_S^* and 0.6 s in Δt_P^*. Further south, Δt^* changes gradually back to higher attenuation south of the Border Ranges Fault. The patterns show little difference with east/west back-azimuth, consistent with a putative slab structure with roughly east-west strike.

In cross section (**Figure 10**) the northern low-attenuation region lies above where the slab is approximately 40 – 110 km deep, with Δt^* substantially increasing farther north. The region of high Δt^* located south of the Border Ranges fault does not have an analog in the Alaska-Aleutian subduction region, and may relate to unusual structure of the Yakutat collision south of that fault zone. Overall the attenuation measurements have a clearer relationship to shallow subduction geometry here than travel times, which are generally slow throughout.

4.5 Regions 2 & 6 - The Cook Inlet Basin and the Yakutat Terrane sediments

Region 6 is dominated by the Yakutat basin, a marine sedimentary section approximately 10 km thick (Trop & Ridgway, 2007) associated with very low crustal velocities (Berg et al., 2020). Slow arrivals in this region are partly due to the thick sedimentary section; on average this is the slowest region within the study area with ΔT_S & ΔT_P of 1.67 ± 0.03 s and 0.58 ± 0.02 s respectively, and shows little dependence on back azimuth. The Cook Inlet Basin, Region 2, contains a sedimentary cover sequence reaching depths approximately 8 km at its deepest parts (Plafker & Berg, 1994; Shellenbaum et al., 2010; Smith & Tape, 2020), and substantially delayed arrivals relative to surrounding regions, by 0.81 s and 0.27 s for ΔT_S and ΔT_P, respectively.

By contrast, the Δt^*measurements show little clear correlation with the presence of thick sediment sequences. In the Yakutat region (Region 6) Δt_P^* shows variable values that average near zero, while Δt_S^* is moderately positive (0.29 ± 0.02 s) (**Table 1; Figure 3**). Within the Cook Inlet basin (Region 2) mean Δt^*reaches the most negative values of any region (-0.35 ± 0.01 and -0.94 ± 0.04 for *P* and *S* respectively). We note that this basin also lies above a cold subducting plate.

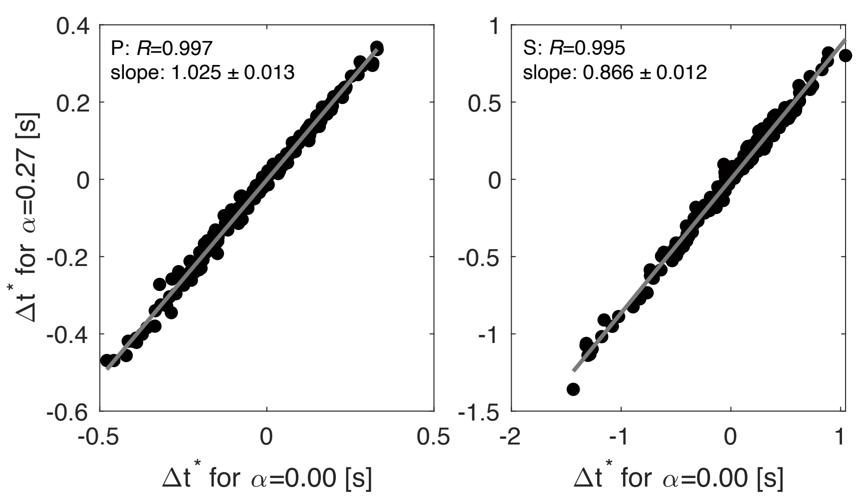

Figure 11. *Comparison of differential attenuation measurements for assumption of frequency independence (horizontal axis) or assuming weak frequency dependence of α = 0.27. Left: P waves. Right: S waves.*

4.6 Variation with frequency dependence

We calculate Δt^* assuming frequency independence ($\alpha = 0$) in most of the results presented here, but also test a weak frequency dependence of $\alpha = 0.27$ for comparison to previous attenuation studies (e.g., Abers et al., 2014). The frequency-dependent attenuation operators Δt^*_{0ij} are effectively the attenuation at 1 Hz, under the assumption that the frequency dependence holds between the frequencies of measurement (0.05 – 0.5 Hz) and 1 Hz. The two estimates (for $\alpha = 0$ and $\alpha = 0.27$) are highly correlated with correlation coefficients R of 0.997 and 0.995 for P and S respectively (**Figure 11**). For *P* waves the two sets are equal within uncertainty, while Δt^*_S for $\alpha = 0.27$ are 86 ± 1 % of those for $\alpha = 0$. The slight decrease in apparent attenuation is consistent with attenuation at the highest frequencies controlling the Δt^* estimates (Stachnik et al., 2004), which in this case is 0.5 Hz, as $(0.5/1.0)^{0.27} = 83\%$, approximately what is observed.

5. Discussion

5.1. Sources of attenuation or velocity anomalies

In the Alaskan-Aleutian subduction region, relatively slower arrivals (larger ΔT) occur northwest of the arc (Region 1) compared to the forearc (Region 3), consistent with subduction of a cold, fast plate beneath a warm backarc asthenosphere. This feature has been seen in local (e.g., Kissling & Lahr, 1991; Zhao et al., 1995; Nayak et al., 2020) and teleseismic tomography (e.g., Martin-Short et al., 2018; Gou et al., 2019; Frost et al., 2020). In comparison, Δt^* shows the transition from low forearc attenuation to high attenuation farther southeast and much closer to the arc, near the 75 km slab contour (**Figure 9**). The Δt^* pattern closely matches that seen in local-earthquake attenuation studies (Stachnik et al., 2004; Mann & Abers, 2020), supporting the suggestion that the mantle wedge above the downgoing plate controls teleseismic body wave attenuation.

One explanation for the difference between travel-time and attenuation patterns is that they are sensitive to underlying mechanisms with different characteristic depths. The Δt^* results are best explained if attenuation is most sensitive to high temperature near the solidus, which is likely achieved at a relatively confined depth range near 50 km where much melt equilibrates in arcs (e.g., Lee et al., 2009). By contrast, the elastic or anharmonic contribution of temperature to V_S remains roughly constant at all temperatures, so would be strongly affected by the contrast between cold slabs and hot surrounding mantle at all depths. Recent experiments indicating strong sensitivity of attenuation to near-solidus conditions (Yamauchi & Takei, 2016; Takei, 2017) or to small degrees of melt just above the solidus (Faul et al., 2004). Depth-dependent attenuation estimates in Tonga (Wei & Wiens, 2018) support a shallow-mantle origin for the strongest attenuation anomalies near arcs. To emphasize this point, **Supplemental Text S3** and **Figure S3** show estimates of the accumulated velocity difference (i.e., ΔT) and attenuation difference (Δt^*) between a cold slab-like geotherm and adiabatic mantle wedge, assuming the calibration of Yamauchi & Takei (2016; Takei, 2017). This calculation shows that Δt^* is controlled almost entirely by temperature in the upper 150-200 km while ΔT depends on thermal contrasts throughout the upper mantle. Note that this analysis does not account for any additional anelastic effects owing to *in situ* melt (Faul et al., 2004), which is also thought to be confined to the upper 200 km of mantle (e.g., Hirschmann, 2006). Thus, the differences measured in this study between integrated attenuation and velocity anomalies are likely a consequence of the different depth distributions of elastic and anelastic effects.

Similar to the Alaska-Aleutian arc, patterns of low attenuation in the WVF provide evidence for subduction. The ΔT anomalies (**Figure** 4) show fast arrivals in P and S persisting hundreds of km north of the WVF, particularly for west back-azimuths (Figure 8c,d) consistent with a deep aseismic extension of the slab here similar to that imaged west of Cook Inlet. By contrast, a northward transition from low attenuation (negative Δt^*) to high occurs almost directly beneath the WVF volcanoes (**Figure 10).** This pattern resembles that seen in Cook Inlet (**Figure 9**), although the extrapolation of the surface gradient downwards intersects the Wrangell slab surface at slightly greater depths. This pattern is consistent with a hot mantle wedge north of the cold subducting Yakutat lithosphere beneath the WVF. Again, the differences are consistent with attenuation being more sensitive to shallow mantle features while travel times integrate deeper structure.

5.2 Evidence for Wrangell subduction in the continental interior

In the Continental Interior region (Region 4), east and north of the Aleutian WBZ intermediate-depth seismicity, some velocity imaging studies show a high-velocity subducting slab extending east of the edge of the WBZ seismicity (Wang & Tape 2014; Jiang et al., 2018), while others do not (Martin-Short et al., 2018; Berg et al., 2020). On average, the continental interior shows the highest Δt^* (most attenuation) of any region (**Table 1**). This broad swath of high attenuation extends the Arc/Backarc region (Region 1) east along strike, suggesting a similar origin. The high attenuation northwest of Cook Inlet appears to stem from mantle wedge processes related to sub-arc melt production, suggesting that high attenuation east of 147°E may likewise result from Yakutat slab subduction beneath the WVF.

In the Cook Inlet region (**Figure 9**) and the Denali segment (Stachnik et al., 2004), low attenuation occurs at stations overlying slab depths of < 80 km. The WVF region shows similarly low attenuation north of where the slab descends to mantle depths (> 40 km), and then manifests a transition to higher attenuation at a slab depth of ~100 km. Intermediate-depth seismicity in both regions confirms the presence of the slab (Page et al., 1989; Ratchkovski & Hansen, 2002). Thus, seismic attenuation in the WVF corridor shows clear evidence of a cold shallow forearc abutting a deeper hot wedge, characteristics of subduction zones worldwide (Abers et al., 2017, 2020).

Still, the Yakutat-Wrangell segment shows complexity not seen in the “normal” subduction segment farther west. There is a zone of high attenuation directly south of the WVF between the Border Ranges Fault and Contact Fault (**Figure 10**) that corresponds to interplate seismicity at depths of 25 – 40 km. This relatively high-attenuation region near 61°N, 145°W extends eastward in Δt_S^* but not Δt_P^* (**Figure 3**), complicating interpretation, and travel times are not informative here due to the large E-W gradient discussed above. This is the one region where the attenuation signal does not have a clear relationship with upper-mantle thermal structure, and may indicate complex crustal processes related to the Yakutat collision here.

Overall, the teleseismic Δt^* results strongly resemble local earthquake attenuation (Stachnik et al. 2004) but provide much wider areal coverage. This study also benefits from the WVLF and SALMON seismic array data that boosts resolution in two critical regions, showing that the pattern in teleseismic attenuation generally resembles that seen from local earthquake data in subduction zones worldwide.

5.3 Sedimentary Structures - Attenuation and Travel Times

The Cook Inlet Basin (Region 2) shows more positive (late) ΔT compared with surrounding regions, consistent with the thick sequence of low-velocity sediments. However, Δt^* is negative in the same place and reaches some of its most negative values throughout the study area, indicating very little (or negative) attenuation. A similar, although less striking, pattern is seen in the shallower Copper River Basin (**Figure 1**), where positive (slow) ΔT is accompanied by negative (less attenuating) Δt^*. The thick pile of Tertiary sediments in the Yakutat area (Region 6) shows very slow travel times, and moderate attenuation, in a pattern that has some similarities although overall slower and more attenuating.

The influence of sediments from the Cook Inlet Basin and Yakutat Terrane (Plafker & Berg 1994; Smith & Tape, 2020) on travel times can be easily explained. In the Cook Inlet Basin, a 5 km sequence with mean S-wave velocity (V_S) of 2.2 km/s surrounded by basement of 3.5 km/s would explain the observed 1.0 s difference in ΔT_S between regions 3 and 2. The P-wave velocity (V_P) has been observed to vary from about 5.0 in the basin to 6.5 km outside, averaged over the upper 10 km (Nayak et al., 2020). That difference explains the 0.35 – 0.40 s difference in ΔT_P observed between the two regions.

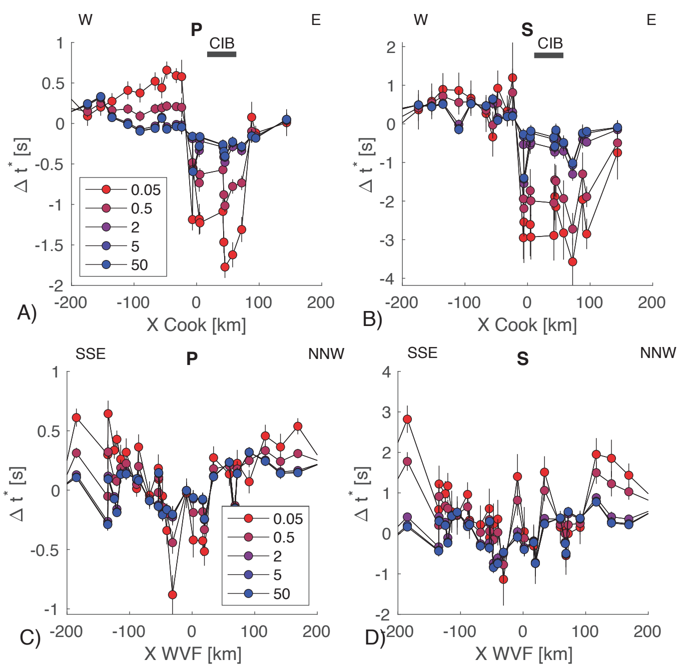

Figure 12. *Attenuation operators along dense transects, varying the weight, A, of fitting amplitude spectra relative to phase spectra. Smaller A, indicated by legend, corresponds to increased fitting of phase terms. A) P-wave results along the Cook Inlet transect (Fig. 9). B) S-wave results along the Cook Inlet transect. C) P-wave results along the Wrangell Volcanic Field transect (Fig. 10). D) S-wave results along the Wrangell Volcanic Field transect. CIB: Cook Inlet Basin. Stations shown all lie within 50 km of the cross section lines shown on Figure 1; lines are same as Figures 9, 10.*

Very low attenuation (negative Δt^*) in the basins is harder to understand. The increased attenuation typically associated with porous sediments at high frequencies (e.g., Müller et al., 2010), does not seem to be a factor here for 0.05 - 0.5 Hz teleseismic body waves. Wavelengths for S waves exceed basin thickness in our attenuation measurement band, so direct basin effects may be minor at finite frequencies. The Cook Inlet Basin sits in the cold part of the forearc typically associated with very low temperatures and little attenuation (Abers et al., 2014; 2017). It is possible that the low attenuation seen here is just an effect of the underlying plate. However, the attenuation is not just low in the basins but also slightly lower than on either side (e.g., **Figures 3, 4**), suggesting additional factors.

Perhaps, basin amplification effects are altering the spectra in ways not accounted for by the attenuation model (equations 2-5). Frequency-dependent amplification has been well documented in the Cook Inlet basin and to lesser extents in other Alaska basins (Moschetti et al., 2020), showing 6 – 14 db S-wave amplification in the 0.1 – 0.5 Hz frequency band (Smith & Tape, 2020). To test the effects of possible amplification, we re-ran the spectral fits varying the weighting factor A between fits to amplitude and phase (equation 6). Basin resonance effects could be altering amplitudes in a manner that steepens the spectral slope and hence mimics negative differential attenuation, but it seems unlikely that they would be altering the phase spectra in the same way. However, we find that increasing the weight on fitting phase spectra ($A < 1.0$) actually exaggerates the negative Δt^* anomaly associated with the Cook Inlet Basin, indicating that the phase spectra are consistent in sign (i.e., spectral slope direction) with amplitude spectra, although scatter increases (**Figure 12**). This pattern indicates that higher frequencies are delayed relative to the low-frequency arrival beyond the physical dispersion associated with the amplitude decay, giving the appearance of additional attenuation in phase compared to that inferred from amplitude decay. Possibly, short-scale wavefront healing at low frequencies could effectively speed up longer periods; additional modeling would be necessary to test this possibility.

Finally, we note that the Cook Inlet Basin shows substantial back-azimuthal variation, perhaps indicative of strong azimuthal anisotropy which might substantially affect attenuation measurements in unexpected ways. ΔT for both P and S is markedly slow in this region for eastern arrivals, and much less so for western arrivals. The sharp gradients in ΔT at the edge of the basin confirm that this signal has a shallow origin. Unfortunately, a lack of usable attenuation measurements from eastern back azimuths precludes a clear picture of how this anisotropy might affect Δt^* values. If anisotropic Q and velocity are correlated here, however, the inhomogeneity in back azimuths for attenuation measurements may exaggerate the amplitude of the low attenuation values measured in this basin.

These findings confirm that sedimentary basins complicate use of teleseismic attenuation measurements. Still, the attenuation signal preserves the essential nature of the underlying mantle thermal structure, unlike the travel times.

5.4 Estimates of Q^{-1}

To compare with laboratory and other seismic measurements, we convert the station-averaged Δt^* to path-averaged $\bar{Q}^{-1}$ beneath each station, from the integrated absorption $t^* = L/\bar{Q}V$. We assume the relevant path length L over which Q varies is the ray path between the base of the crust (30 km depth) and the base of the low-velocity zone (220 km depth), with constant V_P = 8.05 km/s and V_S = 4.45 km/s from PREM (Dziewonski & Anderson, 1981), and typical a teleseismic incidence angle (29°). To convert differential Δt^* to path-integrated t^* we assume $t^* = \Delta t^* + \Delta t^*_{ref}$ where Δt^*_{ref} corresponds to the value that would be estimated for paths with no attenuation in the relevant depth range (Eilon & Abers, 2017). To account for measurement error, Δt^*_{ref} is chosen as the observed value that lies lower than 95% of all station-averaged Δt^* for either *P* or *S* (**Figure 13**), under the assumption that cold slab paths have negligible attenuation in the upper 220 km. This analysis uses only stations that lie outside of the Cook Inlet Basin (Region 2) and the Bristol Bay Basin (stations west of 157°W), to avoid the basin effects discussed above.

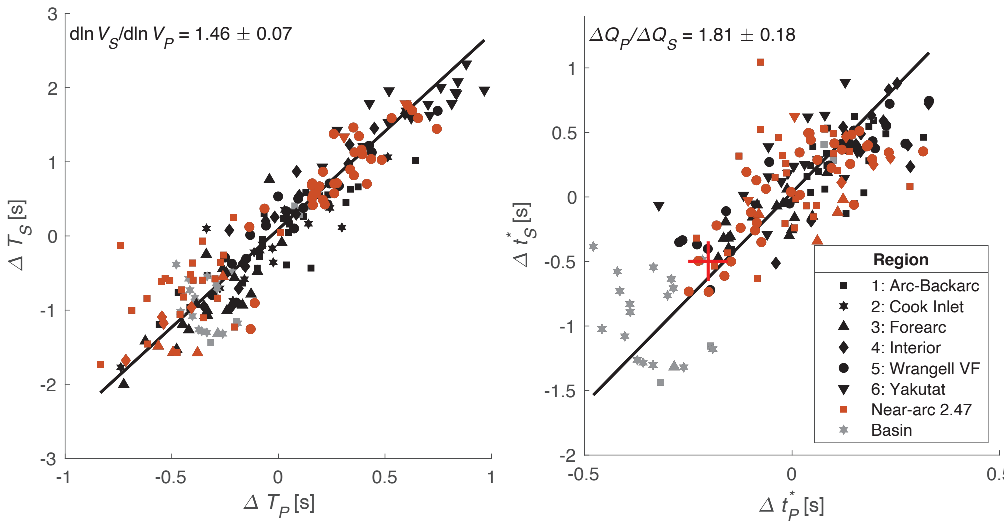

Figure 13. *(Left) Station-averaged P vs. S differential travel times. (Right) Station-averaged P vs. S differential attenuation. Symbols indicate region as shown in legend. Gray symbols: stations in Cook Inlet or Bristol Bay basins; red symbols: stations within 100 km of the arc volcanoes or 100 km WBZ isobath. Line shows orthogonal regression through full dataset; inferred slope (divided by Vp/Vs) shown in upper left, with 95% uncertainties from bootstrap.*

Table 2. Regional regressions on ΔT and Δt^*

Region	Name	dQ_P/dQ_S (1)	dlnV_S/dlnV_P (1)	$1000/\bar{Q}_P$ (2)	$1000/\bar{Q}_S$ (2)
-	All	1.81 ± 0.19	1.46 ± 0.06	-	-
-	No Basin	1.85 ± 0.19	1.46 ± 0.07	8.82 ± 0.07	13.02 ± 0.1
1	Arc/backarc	2.87 ± 1.15	1.21 ± 0.18	9.43 ± 0.19	14.00 ± 0.31
2	Cook Inlet	-	1.36 ± 0.30	-	-
3	Forearc	2.05 ± 0.74	2.14 ± 0.66	6.02 ± 0.32	6.81 ± 0.30
4	Cont. Int.	2.82 ± 1.55	1.58 ± 0.15	14.22 ± 0.34	18.37 ± 0.72
5	Wrangell	1.47 ± 0.18	1.61 ± 0.27	8.04 ± 0.24	11.93 ± 0.32
6	Yakutat	2.09 ± 1.16	0.89 ± 0.22	7.33 ± 0.44	15.47 ± 0.63
7	Near-arc	2.47 ± 0.78	1.44 ± 0.12	8.10 ± 0.14	12.10 ± 0.22

(1) Estimates assume $V_P/V_S = 1.81$, from orthogonal regression. Uncertainties are 2-σ from bootstrap. Results excluded where uncertainty exceeds 2.0. Region 2 was removed from *Q* estimates.
(2) $1000/\bar{Q}$ are path averages over upper 220 km as described in text, with 2-σ uncertainties in mean

The full non-basin dataset gives mean $1000/\bar{Q}$ as 8.8 ± 0.1 or 13.0 ± 0.1 for *P* and *S* respectively (2-σ uncertainties in means). These same data give median quality factors of $\bar{Q}_P$ = 109 and $\bar{Q}_S$ = 70. These estimates vary regionally (**Table 2**); for example, $1000/\bar{Q}_S$ varies from 6.8 ± 0.3 to 14.0 ± 0.3 ($\bar{Q}_S$ varies between 147 and 71) between the forearc (Region 3) and backarc (Region 1). Much stronger attenuation ($1000/\bar{Q}_S$ ~ 40) is inferred from a similar calculation beneath the Juan de Fuca ridge where substantial melt is present (Eilon & Abers, 2017). These absolute values are similar to global and regional surface-wave studies of the uppermost mantle, which show global average $1000/\bar{Q}_S \sim 12 - 15$ at 100 – 200 km depth, varying from 8 to 16 with tectonic region (e.g., Dalton et al., 2008). Surface waves sample roughly 10× longer periods than the teleseismic body waves here, indicating a fairly minimal frequency dependence ~100 s and ~10 s period. However, different regions are averaged in this comparison so some frequency dependence may be balanced by regional variation. Also, the choice of Δt^*_{ref} is somewhat ad hoc; choosing the lowest observed Δt^* rather than the 5th percentile will reduce Δt^*_{ref} by 0.24 s and increase the mean $1000/\bar{Q}_S$ by 4.9.

High-frequency local body wave estimates (assuming frequency independence) show $1000/\overline{Q_S}$ of 3 – 4.5 for paths in the Denali segment (Stachnik et al., 2004). These paths have geometries that are analogous to those here, but indicate 3 – 5 times lower $1000/\overline{Q_S}$. Those measurements are most sensitive to frequencies near 10 Hz, which are 30±10 times higher than the maximum frequencies sampled here. The difference in attenuation could be explained by a frequency dependence of f^{α} where $\alpha = 0.3 - 0.5$ (since $30^{0.3-0.5} = 2.8 - 5.5$). That α is slightly larger than determined experimentally (Jackson & Faul, 2010; Takei, 2017) but the paths are not identical. Alternatively, the Cook Inlet and Wrangell regions may have quantitatively higher attenuation than the Denali segment, a consequence of more abundant melt as reflected by extensive volcanism. Other volcanically productive arcs show high-frequency attenuation more similar to the teleseismic estimates here. For example, in the Mariana back-arc means Pozgay et al. (2009) estimated a maximum $1000/Q_S$ of 30, and Rychert et al. (2008) estimated $1000/Q_S$ of 23 and 15 beneath Nicaragua and Costa Rica respectively. Overall, the most attenuating regions here are quantitatively consistent with a wide variety of other subduction zone studies. Future work would be needed to more carefully account for regional variability and the role of frequency dependence.

5.5 Covariance between *P* and *S* measurements

The covariation of ΔT for *P* and *S* provides a measurement of $d(\ln V_S)/d(\ln V_P)$, the covariation of *S* with *P* velocities. That can offer insight into the processes that cause elastic moduli to vary. At one extreme the bulk and shear moduli can vary similarly such that $d(\ln V_S)/d(\ln V_P) \sim 1 - 1.5$, as expected for anharmonic temperature variations or some melt fabrics, while near-solidus temperature variations or high-aspect-ratio fluid distribution lead to stronger shear modulus reduction than bulk modulus, with $d(\ln V_S)/d(\ln V_P) \geq 2$ (e.g., Karato, 1993; Takei, 2002). Similarly, covariation between Δt^*_P with Δt^*_S provides a measurement of the relative variation of the *P* and *S* attenuation dQ_P/dQ_S (see Supplemental Information). For attenuation in shear modulus only, dQ_P/dQ_S should be $4/3(V_S/V_P)^2$, or 2.25 – 2.43 for V_P/V_S = 1.73 – 1.81, whereas lower values of this ratio indicate bulk attenuation is significant.

For the entire dataset, we find $d(\ln V_S)/d(\ln V_P) = 1.46 \pm 0.07$ (95% uncertainties from bootstrap), consistent with thermal or equilibrated melt processes, and $dQ_P/dQ_S = 1.85 \pm 0.19$ (1.81 ± 0.18 when basins are included; **Table 2**) indicating some relaxation of bulk moduli (**Figure 13**). These correlations lie within the range of similar observations at other subduction zones, some of which also indicate the possibility of bulk attenuation (e.g., Wei & Wiens, 2020). Bulk attenuation may be a common feature of subduction systems. The different raypaths contributing to this array average sample subducting lithosphere, back-arc mantle, and subcontinental mantle so it is difficult to be sure exactly where the bulk attenuation occurs. If the data are limited to stations near the volcanic arcs (within 100 km of a volcano or the 100-km

WBZ contour on **Figure 1**), we find dQ_P/dQ_S = 2.47 ± 0.78 (Near-arc in **Table 2**). This variation allows the possibility that all variation is in the shear modulus in the subduction mantle wedge, although uncertainties are large. The range of values in ΔT or Δt_P^* are too limited within any other single subregion to obtain regression with smaller uncertainties, although some variations exist (Soto Castaneda, 2020; Supplemental Information). In particular, high dQ_P/dQ_S is associated with the backarc Regions 1 and 4, indicating that the high attenuation there is a shear-modulus-controlled process. Bulk attenuation is only indicated for Region 5, coincident with the WVF, where extensive melt transport may be occurring (see Supplemental Information Text S2).

6. Conclusions

Teleseismic body-wave attenuation varies substantially across the Alaska subduction zones. Our results agree with previous local earthquake attenuation measurements where they overlap spatially, and complement teleseismic velocity studies. Specifically, the Δt^* measurements show a boundary between the hot mantle wedge and the cold forearc in both the Alaska-Aleutian system and the Yakutat subduction system. The former matches well the observations from local-earthquake attenuation studies in the Cook Inlet and Denali regions of a boundary near where the subducting plate interface reaches 75 km depth. The presence of a similar feature beneath the Wrangell Volcanic Field provides evidence for typical subduction thermal structure. These measurements contrast with ΔT, which shows high-velocity slabs extending to depths past WBZ seismicity but relatively little evidence for the shallow hot mantle wedge. That difference is likely due to the importance of near-solidus temperatures in reaching high $1/Q$, a condition that exists largely in the upper 150-200 km. Velocity shows sensitivity to temperatures even far from the solidus, so ΔT has sensitivity to deeper structure in subduction zones.

Travel times and attenuation measurements also differ in their sensitivity to the presence of sedimentary basins. While low-velocity sediments have a first-order effect to delay ΔT measurements the teleseismic Δt^*measurements show no evidence of increased attenuation over basins, at the low frequencies of these signals. In fact, the Cook Inlet Basin shows the most negative $\Delta t^*$of any region from both the amplitude and phase spectra, suggesting the possibility of some sort of frequency-dependent phase delay mimicking negative differential attenuation here.

Attenuation is of the order $1000/Q_S$ ~ 8-15 averaged over the upper 220 km of mantle. These measurements, dominated by frequencies of 0.2-0.5 Hz, are comparable to the global variations seen in surface-wave attenuation at these depths, and somewhat higher than inferred in the nearby Denali region from higher-frequency body waves. Some of that difference may reflect differences between the Cook Inlet and amagmatic Denali segment, as high-frequency measurements from other subduction zones are similar to the teleseismic measurements obtained here, and some frequency dependence may contribute. Uncertainties in the actual depth range and geographic area controlling the observed signals make direct comparisons difficult.

Correlations between ΔT_P and ΔT_S, or between Δt_P^* and Δt_S^*, provide some evidence for the physical mechanisms giving rise to observed velocity and attenuation anomalies. Across the array the measurements give $d(\ln V_S)/d(\ln V_P)$ ~ 1.46 consistent with thermal processes and textural equilibrium in melt-rich areas. The attenuation measurements give dQ_P/dQ_S that require some bulk-modulus relaxation over the whole region, although the near-arc region are consistent with only shear attenuation.

Overall, the large-scale patterns seen here resemble those inferred from local-earthquake studies, suggesting that teleseismic measurements such as these provide useful complements to velocity imaging in subduction zones, particularly for the uppermost mantle.

Acknowledgments and Data Availability

This research was supported by the National Science Foundation award EAR-1460291. New data collection for the WVLF experiment was supported by the IRIS-PASSCAL Instrument Center, which provided excellent logistical and technical support. *Data Availability:* All waveform data are archived and openly available at the IRIS Data Management Center (www.iris.edu/ds), under station code YG (2016-18) for WVLF (Christensen & Abers, 2016; https://doi.org/10.7914/SN/YG_2016), ZE (2015-17) for SALMON (Tape et al., 2017; https://doi.org/10.7914/SN/ZE_2015), and TA for the Alaska Transportable Array (IRIS Transportable Array, 2003; https://doi.org/10.7914/SN/TA). We thank C. Tape for making SALMON data available prior to its release.

References

Abers, G.A., Fischer, K.M., Hirth, G., Wiens, D.A., Plank, T., Holtzman, B.K., McCarthy, C., and Gazel, E., 2014, Reconciling mantle attenuation-temperature relationships from seismology, petrology and laboratory measurements: Geochem. Geophys. Geosys. (G3), v. 15, p. 3521–3542, doi:10.1002/2014GC005444.

Abers, G.A., van Keken, P.E., and Hacker, B.R., 2017, The cold and relatively dry nature of mantle forearcs in subduction zones: Nature Geosci., v. 10, p. 333–337, doi:10.1038/NGEO2922.

Abers, G.A., van Keken, P.E., and Wilson, C.R., 2020, Deep decoupling in subduction zones: Observations and temperature limits: Geosphere, v. 16, doi:10.1130/GES02278.1.

Anderson, D.L., and Minster, J.B., 1979, The frequency dependence of Q in the Earth and implications for mantle rheology and Chandler wobble: Geophysical Journal of the Royal Astronomical Society, v. 58, p. 431–440.

Berg, E.M., Lin, F., Allam, A., Schulte-Pelkum, V., Ward, K.M., and Shen, W., 2020, Shear Velocity Model of Alaska Via Joint Inversion of Rayleigh Wave Ellipticity, Phase Velocities, and Receiver Functions Across the Alaska Transportable Array: Journal of Geophysical Research: Solid Earth, v. 125, p. e2019JB018582.

Bezada, M., Byrnes, J., and Eilon, Z., 2019, On the robustness of attenuation measurements on teleseismic P waves: insights from micro-array analysis of the 2017 North Korean nuclear test: Geophysical Journal International, v. 218, p. 573–585. http://doi.org/10.1093/gji/ggz169

Brueseke, M.E., Benowitz, J.A., Trop, J.M., Davis, K.N., Berkelhammer, S.E., Layer, P.W., and Morter, B.K., 2019, The Alaska Wrangell Arc:~ 30 Ma of subduction-related magmatism along a still active arc-transform junction: Terra Nova, v. 31, p. 59–66.

Bruns, T.R., R. von Huene, R. C. Culotta, S. D. Lewis, and J. W. Ladd, 1987, Geology and petroleum potential of the Shumagin margin, Alaska, *in* D. W. Scholl, A. G. Grantz, and J. G. Vedder eds., Geology and Resource Potential of the Continental Margin of Western North America and Adjacent Ocean Basins -- Beaufort Sea to Baja California, Circum-Pacific Council on Energy and Mineral Resources Ear. Sci. Ser., vol. 6, Tulsa, A.A.P.G., p. 157–189.

Buurman, H., Nye, C.J., West, M.E., and Cameron, C., 2014, Regional controls on volcano seismicity along the Aleutian arc: Geochem. Geophys. Geosys. (G3), v. 15, p. 1147–1163, doi:10.1002/2013GC005101.

Christensen, D., and G. Abers (2016). *Fate and consequences of Yakutat terrane subduction beneath eastern Alaska and the Wrangell Volcanic Field*. International Federation of Digital Seismograph Networks. https://doi.org/10.7914/SN/YG_2016

Christeson, G.L., Gulick, S.P.S., van Avendonk, H.J.A., Worthington, L.L., Reece, R.S., and Pavlis, T.L., 2010, The Yakutat terrane: Dramatic change in crustal thickness across the Transition fault, Alaska: Geology, v. 38, p. 895–898, doi:10.1130/g31170.1.

Dalton, C.A., Ekström, G., and Dziewonski, A.M., 2009, Global seismological shear velocity and attenuation: a comparison with experimental observations: Earth Planet. Sci. Lett., v. 284, p. 65–75.

Daly, K.A., G.A. Abers, S. Roecker, M.E. Mann and D.H. Christensen, 2019, A Wadati-Benioff zone beneath the Wrangell Volcanic Field revealed by the WVLF broadband array, *Abstr. T41F-0298*, Amer. Geophys. Un. 2019 Fall Meeting, San Francisco, 9-13 Dec.

Dziewonski, A., S. Bloch, and M. Landisman, 1969, A technique for the analysis of transient seismic signals: Bull. Seism. Soc. Am., v. 59, p. 427–444.

Dziewonski, A.M., and D. L. Anderson, 1981, Preliminary reference Earth model: Phys. Earth Planet. Inter., v. 25, p. 297–356.

Eberhart-Phillips, D., Christensen, D.H., Brocher, T.M., Hansen, R., Ruppert, N.A., Haueussler, P.J., and Abers, G.A., 2006, Imaging the transition from Aleutian subduction to Yakutat collision in central Alaska, with local earthquakes and active source data: J. Geophys. Res., v. 111, p. B11303, doi:10.1029/2005JB004240.

Eilon, Z.C., 2016, New Constraints on Extensional Environments through Analysis of Teleseisms [PhD]: Columbia Univ., 217 p.

Eilon, Z.C., 2016, New Constraints on Extensional Environments through Analysis of Teleseisms [PhD]: Columbia Univ., 217 p.

Eilon, Z.C., and Abers, G.A., 2017, High seismic attenuation at a mid-ocean ridge reveals the distribution of deep melt: Science Advances, v. 3, p. e1602829.
Elliott, J., and Freymueller, J.T., 2020, A Block Model of Present-Day Kinematics of Alaska and Western Canada: Journal of Geophysical Research: Solid Earth, p. e53951.
Faul, U.H., FitzGerald, J.D., and Jackson, I., 2004, Shear wave attenuation and dispersion in melt-bearing olivine polycrystals: 2. Microstructural interpretation and seismological implications: J. Geophys. Res., v. 109, p. B06202, doi:10.1029/2003JB002407.
Faul, U.H., and Jackson, I., 2005, The seismological signature of temperature and grain size variations in the upper mantle: Earth Planet. Sci. Lett., v. 234, p. 119–134, doi: 10.1016/j.epsl.2005.02.008.
Ferris, A., G. A. Abers, D. H. Christensen, and E. Veenstra, 2003, High resolution image of the subducted Pacific (?) plate beneath central Alaska, 50-150 km depth: Earth Planet. Sci. Lett., v. 214, p. 575–588.
Frost, D.A., Romanowicz, B., and Roecker, S., 2020, Upper mantle slab under Alaska: contribution to anomalous core-phase observations on south-Sandwich to Alaska paths: Physics of the Earth and Planetary Interiors, v. 299, p. 106427.
Gou, T., Zhao, D., Huang, Z., and Wang, L., 2019, Aseismic deep slab and mantle flow beneath Alaska: Insight from anisotropic tomography: Journal of Geophysical Research: Solid Earth, v. 124, p. 1700–1724, doi:10.1029/2018JB016639.
Hammond, W.C., and E. D. Humphreys, 2000a, Upper mantle seismic wave velocity: effects of realistic partial melt geometries: J. Geophys. Res., v. 105, p. 10,975-10,986.
Hammond, W.C., and E. D. Humphreys, 2000b, Upper mantle seismic wave attenuation: effects of realistic partial melt distribution: J. Geophys. Res., v. 105, p. 10987–10999.
Hirschmann, M.M., 2006, Water, melting, and the deep earth H2O cycle: Ann. Rev. Earth Planet. Sci., v. 34, p. 629–653.
IRIS Transportable Array. (2003). USArray Transportable Array. International Federation of Digital Seismograph Networks. https://doi.org/10.7914/SN/TA
Jackson, I., and Faul, U.H., 2010, Grainsize-sensitive viscoelastic relaxation in olivine: Toward a robust laboratory-based model for seismological application: Phys. Earth Planet. Int., v. 183, p. 151–163, doi:https://doi.org/10.1016/j.pepi.2010.09.005.
Jiang, C., Schmandt, B., Ward, K.M., Lin, F., and Worthington, L.L., 2018, Upper mantle seismic structure of Alaska from Rayleigh and S wave tomography: Geophysical Research Letters, v. 45, p. 10–350.
Karato, S., 1993, Importance of anelasticity in the interpretation of seismic tomography: Geophys. Res. Lett., v. *20*, p. 1623–1626.
Karato, S., 2003, Mapping water content in the upper mantle, *in* Eiler, J.M. ed., Inside the Subduction Factory, Geophys. Monogr. 138, Washington, Am. Geophys. Union, p. 135–152.
Kissling, E., and Lahr, J.C., 1991, Tomographic image of the Pacific slab under southern Alaska: Eclogae Geologicae Helvetiae, v. 84, p. 297–315.
Lee, C.-T.A., Luffi, P., Plank, T., Dalton, H., and Leeman, W.P., 2009, Constraints on the depths and temperatures of basaltic magma generation on Earth and other terrestrial planets using new thermobarometers for mafic magmas: Earth Planet. Sci. Lett., v. 279, p. 20–33.
Li, J., Abers, G.A., Kim, Y.H., and Christensen, D., 2013, Alaska Megathrust 1: Seismicity 43 years after the great 1964 Alaska megathrust earthquake: J. Geophys. Res., v. 118, p. 4861–4871, doi:10.1002/jgrb.50358.
Mann, M.E., and Abers, G.A., 2020, First-order mantle subduction-zone structure effects on ground motion: The 2016 M w 7.1 Iniskin and 2018 M w 7.1 Anchorage earthquakes: Seismological Research Letters, v. 91, p. 85–93.
Martin-Short, R., R. M. Allen, and I. D. Bastow, 2016, Subduction geometry beneath south central Alaska and its relationship to volcanism: Geophys. Res. Lett., v. 43, p. 9509–9517, doi:10.1002/2016GL070580.
Martin-Short, R., Allen, R., Bastow, I.D., Porritt, R.W., and Miller, M.S., 2018, Seismic Imaging of the Alaska Subduction Zone: Implications for Slab Geometry and Volcanism: Geochemistry, Geophysics, Geosystems, v. 19, p. 4541–4560.
McPherson, A., Christensen, D., Abers, G., and Tape, C., 2020, Shear Wave Splitting and Mantle Flow beneath Alaska: Journal of Geophysical Research: Solid Earth, v. 125, p. e2019JB018329.

Moschetti, M.P., Thompson, E.M., Rekoske, J., Hearne, M.G., Powers, P.M., McNamara, D.E., and Tape, C., 2020, Ground-Motion Amplification in Cook Inlet Region, Alaska, from Intermediate-Depth Earthquakes, Including the 2018 M w 7.1 Anchorage Earthquake: Seismological Research Letters, v. 91, p. 142–152.

Müller, T.M., Gurevich, B., and Lebedev, M., 2010, Seismic wave attenuation and dispersion resulting from wave-induced flow in porous rocks—A review: Geophysics, v. 75, p. 75A147-75A164.

Nayak, A., Eberhart-Phillips, D., Ruppert, N.A., Fang, H., Moore, M.M., Tape, C., Christensen, D.H., Abers, G.A., and Thurber, C.H., 2020, 3D Seismic Velocity Models for Alaska from Joint Tomographic Inversion of Body-Wave and Surface-Wave Data: Seismological Society of America, v. 91, p. 3106–3119.

Nye, C., Begét, J.E., Layer, P.W., Mangan, M.T., McConnell, V.S., McGimsey, R.G., Miller, T.P., Moore, R.B., and Stelling, P.L., 2018, Geochemistry of Some Quaternary Lavas from the Aleutian Arc and Mt. Wrangell: Raw Data File RDF 2018-1: State of Alaska, Department of Natural Resources, Division of Geological & Geophysical Surveys, doi: 10.14509/29843.

Page, R.A., C. D. Stephens, and J. C. Lahr, 1989, Seismicity of the Wrangell and Aleutian Wadati-Benioff zones and the North America plate along the Trans-Alaska crustal transect, Chugach mountains and Copper River basin, southern Alaska: J. Geophys. Res., v. 94, p. 16059–16082.

Pavlis, T.L., Picornell, C., Serpa, L., Bruhn, R.L., and Plafker, G., 2004, Tectonic processes during oblique collision: Insights from the St. Elias orogen, northern North American Cordillera: Tectonics, v. 23, p. TC3001, doi:10.1029/2003TC001557.

Plafker, G., and H. C. Berg, 1994, Overview of the geology and tectonic evolution of Alaska, *in* Plafker ed., The Geology of Alaska, The Geology of North America, G-1, Boulder, Colorado, Geol. Soc. Am., p. 989–1021.

Pozgay, S.H., Wiens, D.A., Conder, J.A., Shiobara, H., and Sugioka, H., 2009, Seismic attenuation tomography of the Mariana subduction system: implications for thermal structure, volatile distribution, and slow spreading dynamics: Geochem. Geophys. Geodyn. (G3), v. 10, p. Q04X05, doi:10.1029/2008GC002313.

Preece, S.J., and Hart, W.K., 2004, Geochemical variations in the < 5 Ma Wrangell Volcanic Field, Alaska: implications for the magmatic and tectonic development of a complex continental arc system: 8th international symposium on Deep seismic profiling of the continents and their margins, v. 392, p. 165–191, doi:10.1016/j.tecto.2004.04.011.

Ratchkovski, N.A., and Hansen, R.A., 2002, New Constraints on Tectonics of Interior Alaska: Earthquake Locations, Source Mechanisms, and Stress Regime: Bull. Seismol. Soc. Amer., v. 92, p. 998–1014.

Roth, E.G., D. A. Wiens, L. M. Dorman, J. Hildebrand, and S. C. Webb, 1999, Seismic attenuation tomography of the Tonga back-arc region using phase pair methods: J. Geophys. Res., v. *104*, p. 4795–4809.

Rychert, C.A., Fischer, K.M., Abers, G.A., Plank, T., Syracuse, E., Protti, J.M., Gonzalez, V., and Strauch, W., 2008, Strong along-arc variations in attenuation in the mantle wedge beneath Costa Rica and Nicaragua: Geochem. Geophys. Geosys., v. 9, p. Q10S10, doi:Q10s10 10.1029/2008gc002040.

Shellenbaum, D.P., Gregersen, L.S., and Delaney, P.R., 2010, Top Mesozoic unconformity depth map of the Cook Inlet basin, Alaska: Alaska Division of Geological and Geophysical Surveys Report of Investigations 2010-2.

Smith, K., and Tape, C., 2020, Seismic Response of Cook Inlet Sedimentary Basin, Southern Alaska: Seismological Research Letters, v. 91, p. 33–55.

Soto Castaneda, R.A., 2020, Teleseismic P and S wave attenuation constraints on temperature and melt of the upper mantle in the Alaska subduction zone [MS. Thesis]: Cornell Univ., 112 p.

Stachnik, J.C., Abers, G.A., and Christensen, D., 2004, Seismic attenuation and mantle wedge temperatures in the Alaska subduction zone: J. Geophys. Res., v. 109, p. B10304, doi:10.1029/2004JB003018.

Takei, Y., 2002, Effect of pore geometry on Vp/Vs: From equilibrium geometry to crack: J. Geophys. Res., v. 107, p. doi:10.1029/2001JB000522.

Takei, Y., 2017, Effects of partial melting on seismic velocity and attenuation: A new insight from experiments: Annual Review of Earth and Planetary Sciences, v. 45, p. 447–470.

Tape, C., Christensen, D., Moore-Driskell, M.M., Sweet, J., and Smith, K., 2017, Southern Alaska Lithosphere and Mantle Observation Network (SALMON): A seismic experiment covering the active arc by road, boat, plane, and helicopter: Seismological Research Letters, v. 88, p. 1185–1202.

Trop, J.M., Ridgway, K.D., Glen, J., and O'Neill, J., 2007, Mesozoic and Cenozoic tectonic growth of southern Alaska: A sedimentary basin perspective: Spec. Pap. Geol. Soc. Amer., v. 431, p. 55.

VanDecar, J.C., and Crosson, R.S., 1990, Determination of teleseismic relative phase arrival times using multi-channel cross-correlation and least squares: Bulletin of the Seismological Society of America, v. 80, p. 150–159.

Van Stiphout, A., Cottaar, S., and Deuss, A., 2019, Receiver function mapping of mantle transition zone discontinuities beneath Alaska using scaled 3-D velocity corrections: Geophysical Journal International, v. 219, p. 1432–1446.

Wang, Y., and Tape, C., 2014, Seismic velocity structure and anisotropy of the Alaska subduction zone based on surface wave tomography: Journal of Geophysical Research: Solid Earth, v. 119, p. 8845–8865.

Ward, K.M., 2015, Ambient noise tomography across the southern Alaskan cordillera: Geophysical Research Letters, v. 42, p. 3218–3227.

Wei, S.S., and Wiens, D.A., 2018, P-wave attenuation structure of the Lau back-arc basin and implications for mantle wedge processes: Earth and Planetary Science Letters, v. 502, p. 187–199.

Wei, S.S., and Wiens, D.A., 2020, High Bulk and Shear Attenuation Due to Partial Melt in the Tonga-Lau Back-arc Mantle: Journal of Geophysical Research: Solid Earth, v. 125, p. e2019JB017527, doi:10.1029/2019JB017527.

Worthington, L.L., Van Avendonk, H.J.A., Gulick, S.P.S., Christeson, G.L., and Pavlis, T.L., 2012, Crustal structure of the Yakutat terrane and the evolution of subduction and collision in southern Alaska: Journal of Geophysical Research-Solid Earth, v. 117, p. art. no. B01102, doi:10.1029/2011jb008493.

Yamauchi, H., and Takei, Y., 2016, Polycrystal anelasticity at near-solidus temperatures: J. Geophys. Res., v. 121, p. 7790–7820.

Zhao, D., D. H. Christensen, and H. Pulpan, 1995, Tomographic imaging of the Alaska subduction zone: J. Geophys. Res., v. 100, p. 6487–6504.

Journal of Geophysical Research

Supporting Information for

Teleseismic attenuation, temperature, and melt of the upper mantle in the Alaska subduction zone

Soto Castaneda, R.A.[1], G.A. Abers[1], Z. Eilon[2], and D. H. Christensen[3]

[1]Department of Earth and Atmospheric Sciences, Cornell University, Ithaca NY; [2]Department of Earth Science, University of California, Santa Barbara; [3]Geophysical Institute, University of Alaska Fairbanks

Contents of this file

Supplementary Text S1. Regressions on ΔT_S - ΔT_P and $\Delta t^*_S - \Delta t^*_P$ and their relation to Q, V.
Supplementary Text S2. dQ_P/dQ_S and $\mathrm{dln}V_S/\mathrm{dln}V_P$ estimates for individual regions.
Supplementary Text S3. Predicted depth dependence of Δt^*_S and ΔT_S in subduction zones
Supplementary Text S4. Explanation of columns in Table S1.
Supplementary Figures S1-S3.
Supplementary Table S1. separate text file with station-averaged measurements.

Introduction

This auxiliary material includes details of calculations, text tables and figures related to regressions between P and S quantities not discussed in the text. It provides an expanded theoretical prediction for depth sensitivity of measurements to temperature variations. It also includes the full results table presented as station averages.

S1 Text. Regressions on ΔT_S - ΔT_P and Δt^*_S – Δt^*_P and their relation to Q, V.

Variations in attenuation operator (Δt^*) or travel time (ΔT) between stations can be attributed to differences in attenuation ($1/Q$) or velocity (V) in a volume beneath the array. This simple analysis demonstrates that relationship. We assume that paths from each earthquake are only affected by variations in $1/Q$ or V within that volume shallower than some maximum depth Z, and that V is constant within that volume in the upper mantle. If the array is small enough then ray parameter is also constant, so $Z = L \cos(j)$, where L is the ray path length and j is the ray incidence angle with L the same for all stations. Then, the total travel time T_i and attenuation operator t_i^* are

$$T_i = L/V_i \; + T_{mi}$$
$$t_i^* = L/V_i Q_i + t_{mi}^*$$

where i is P or S, V_i is the path-averaged velocity, Q_i is the path-averaged attenuation operator, and t_{mi}^* and T_{mi} are the contributions from the rest of the path outside the volume of interest.

Travel-time perturbations. We measure ΔT_i (or Δt_i^*), the differences in each quantity between that observed at each station and its network-averaged mean, cancelling t_{mi}^* and T_{mi}. Following the analysis of Koper et al. (1999)

$$T_i = T_{i0} + \Delta T_i$$

which corresponds to a perturbation in velocity

$$\Delta T_i = -L\frac{\Delta V_i}{V_{i0}^2}$$

where V_{i0} is the reference velocity corresponding to the unperturbed travel time $T_{i0} = T_{mi} + L/V_{i0}$. The last equation relies upon Fermat's principle; to first order small changes in V do not alter raypaths (L). Here, the operator Δ represents a small perturbation due to underlying physical processes, such as temperature, melt fraction, or composition, on V_P or V_S. Combining the equations for P and S to eliminate L gives

$$\Delta T_S = \; \Delta T_P \left(\frac{V_{P0}}{V_{S0}}\right) \frac{\Delta V_S/V_{S0}}{\Delta V_P/V_{P0}}\,,$$

which in the limit of infinitesimal perturbations gives the familiar result:

$$\Delta T_S \sim \Delta T_P \left(\frac{V_P}{V_S}\right) \frac{\mathrm{dln}V_S}{\mathrm{dln}V_P}\,.$$

In other words, the slope of a $\Delta T_S - \Delta T_P$ plot gives the proportional velocity perturbation scaled by Vp/Vs.

Attenuation perturbations. Attenuation can be handled similarly, with

$$t_i^* = \frac{L}{V_i}\, q_i + t_{mi}^*$$

where $q_i = 1/Q_i$. Propagating first-order perturbations in q and V,

$$\Delta t_i^* = \frac{L}{V_i}\,\Delta q_i \;+ L q_i\,\Delta(\frac{1}{V_i}) \quad .$$

We can ignore the second term for P waves if

$$|\Delta\left(\frac{1}{V_P}\right) L q_P| \ll |\frac{L}{V_P}\,\Delta q_p|$$

and similar for S. This inequality can be rewritten as

$$|\Delta\left(\frac{L}{V_P}\right)/(\frac{L}{V_P})| \ll |\Delta q_p/q_p|$$

or (to first order)

$$|\Delta(V_P)/(V_P)| \ll |\Delta Q_p/Q_p| \;,$$

which is true in almost all cases. Typically, in the upper mantle $\Delta V/V$ ~ 1-5% while $\Delta Q/Q$ ~ 10-50% (or more). Hence, to a good approximation

$$\Delta t_i^* {\sim} \frac{L}{V_i}\,\Delta q_i$$

leading to the relationship,

$$\Delta t_S^* = \frac{V_P}{V_S}\frac{\Delta q_S}{\Delta q_P}\,\Delta t_P^*$$

or

$$\frac{\Delta(Q_S^{-1})}{\Delta(Q_P^{-1})} \cong \frac{\Delta Q_P}{\Delta Q_S} \cong \frac{V_P}{V_S}\,\frac{\Delta t_S^*}{\Delta t_P^*}\,.$$

Higher-order terms may be significant where $\Delta Q/Q \gg 0$.

Bulk and shear modulus attenuation contributions. It is also useful to compare bulk and shear Q^{-1} by the standard relation (e.g., Anderson & Hart, 1978)

$$Q_P^{-1} = \frac{4}{3}(V_S/V_P)^2 Q_S^{-1} + \left[1 - \frac{4}{3}\left(\frac{V_S}{V_P}\right)^2\right] Q_\kappa^{-1} \quad .$$

In the absence of bulk attenuation (Q_κ^{-1}= 0), this leads to

$$\frac{\Delta t_S^*}{\Delta t_P^*} = \frac{3}{4}\left(\frac{V_P}{V_S}\right)^3$$

which for Vp/Vs = 1.80 gives a slope of 4.37 (or $\Delta Q_P/\Delta Q_S$ = 2.43). For a Poisson solid ($V_P/V_S = \sqrt{3}$) , this gives a slope of 3.90 (or $\Delta Q_P/\Delta Q_S$ = 2.25).

Alternatively, several authors (e.g., Menke & Richards, 1983) have suggested that scattering media have effectively $Q_P = Q_S$, leading to

$$\frac{\Delta t_S^*}{\Delta t_P^*} = \left(\frac{V_P}{V_S}\right)$$

and slopes of 1.80 or 1.73 in the cases above. This is equivalent to $\Delta Q_\mu^{-1} = \Delta Q_\kappa^{-1}$.

Presumably, slopes between 1.80 and 4.37 (or $\Delta Q_P/\Delta Q_S$ between 1.0 and 2.43) reflect intermediate processes, with bulk modulus attenuation variations less than in shear.

Text S2. $\Delta Q_P/\Delta Q_S$ and $\Delta\ln V_S/\Delta\ln V_P$ estimates for individual regions

Regressions between *P* and *S* measurements for the entire dataset constrain $\Delta Q_P/\Delta Q_S$ and $\Delta\ln V_S/\Delta\ln V_P$ as described above. For individual subregions however, regressions result in generally large uncertainties due to the limited range in values and the subsequent lack of leverage on slope (**Figure 13, S1**).

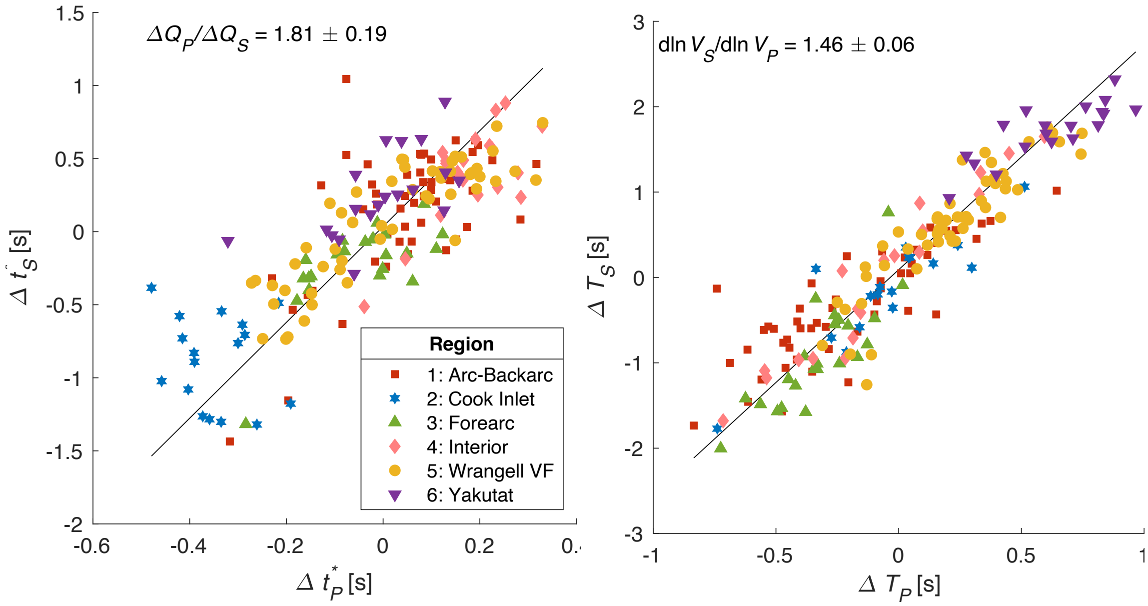

Figure S1. *Correlations between P and S measurements for (left) attenuation operator and (right) travel time variations, highlighting individual regions as indicated by symbol and color (see Key). Similar to Figure 13 in main text.*

To assess slope uncertainties, the slope from orthogonal regressions (allowing uncertainty in both axes) are repeated for 1000 bootstrap trials for each subregion and the central 90% quantile is taken to represent uncertainty (Figure **S2**). Note that region 2 (Cook Inlet) gave a negative slope for $\Delta Q_P/\Delta Q_S$ and is not shown.

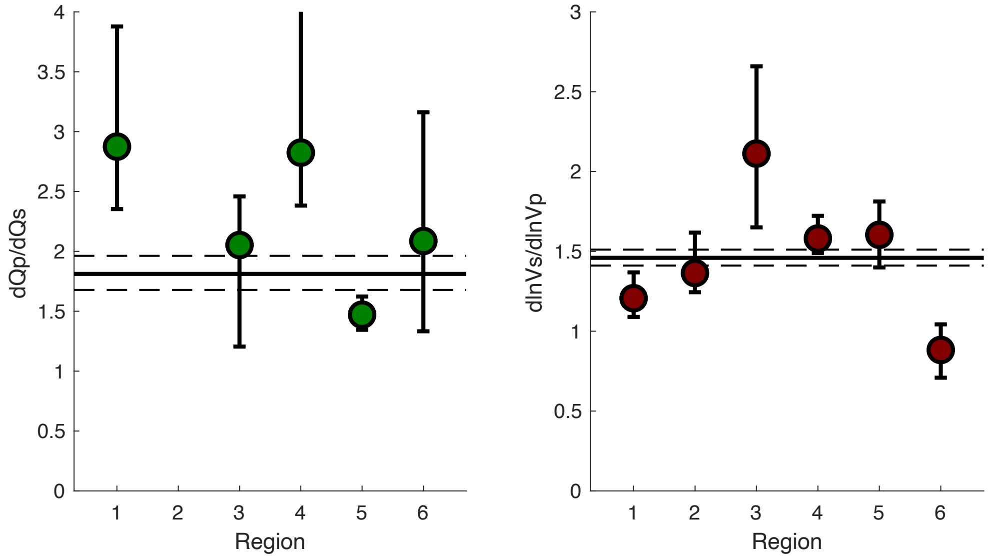

Figure S2. *Estimates for individual subregions of (left) dQp/dQs or (right) dlnVs/dlnVp from attenuation operators or travel times, respectively. Regions are indicated by integer along bottom; see legend in Figure S1 for region names. Circles show best estimates from all stations in that region, and error bars show variation from 1000 bootstrap trials as the central 90% of trials. Horizontal solid line shows regression result for entire dataset, and dashed lines show 90% uncertainty using the same method.*

These estimates show overlap of error bars between regions, with a few exceptions. Region 3 (the Forearc) is the only region with significantly (2-σ) larger $\Delta\ln V_S/\Delta\ln V_P$ than the whole dataset, while Region 6 (Yakutat forearc) is significantly lower. This variation is hard to interpret in terms of subduction-related mantle process, as both regions lie over the cold forearc where the incoming plate lies immediately beneath upper-plate crust. Possibly, the very thick Yakutat sediments play a role, but as indicated in the text there is a large eastward gradient in travel times indicating an effect of deeper low-velocity structures. It will be difficult to assess this variation in $\Delta T_S/\Delta T_P$ without careful tomographic study.

The regional variations in $\Delta Q_P/\Delta Q_S$ are more consistent, with high values (>2.4) mostly in Regions 1 and 4, the two backarc regions, or for the near-arc stations. For these regions it is difficult to reconcile data with any bulk-modulus attenuation, consistent with thermal and/or some melt processes for affecting Q only in shear (e.g., Faul & Jackson, 2005; Hammond & Humphreys, 2000). In one region, Region 5 (Wrangell Volcanic Field), the data require $\Delta Q_P/\Delta Q_S < 1.7$ and so bulk attenuation must be present. This region includes some of the highest Δt_P^* measurements in the entire dataset, consistent with high temperatures and possible melt-related bulk modulus effects similar to those inferred for Tonga (Wei & Wiens, 2020).

Supplementary Text S3. Predicted depth dependence of Δt^*_S and ΔT_S in subduction zones. Lateral temperature variations produce different variations in depth-integrated velocities or attenuation predicted for subduction zones. This discussion focuses on the shear modulus, as bulk-modulus processes are less well understood. Temperature affects V_S through both anharmonic (elastic) processes and anelastic processes via physical dispersion, while Q_S is by definition just a result of anelasticity (e.g., Karato, 1993). The anharmonic derivatives of shear modulus or V_S are nearly linear over a wide range of temperatures, while anelastic effects are largest near the solidus where they are dominated by either pre-melting (Takei, 2017) or very small melt fraction effects (Faul et al., 2004). As a result, attenuation variations are significant between the hot, near-adiabatic mantle wedge and the slab interior at shallow depths where the mantle adiabat lies near its solidus, but not deeper. Velocity variations are more broadly sensitive over a large range of depths and temperatures within the subducting slab.

To illustrate this point, we consider a simple thermal model of a subducting plate that instantaneously enters the mantle at constant dip δ, with an initial linear plate thickness of *a* and a linear geotherm (McKenzie, 1969). Once in the mantle, the top and bottom surface of the plate is fixed at constant ambient temperature T_a. This well-known one-dimensional conductive heating problem has a Fourier series solution. Retaining just the dominant first term, the center of the slab has a temperature of

$$T_{ctr}(z) = T_a\left[1 - \frac{2}{\pi}\exp\left(-\frac{\pi^2 \kappa z}{V a^2 sin\delta}\right)\right]$$

where z is the depth to the top of the plate, V is the rate of plate convergence and κ is the thermal diffusivity. Away from the center the slab is warmer. If we approximate $a \sim 2.32\sqrt{\kappa A}$ for plate age A (Turcotte & Schubert, 2002), then

$$T_{ctr}(z) = T_a\left[1 - \frac{2}{\pi}\exp\left(-\frac{1.83z}{VAsin\delta}\right)\right]$$

and is significantly cooler than the ambient mantle. To evaluate the differences, we compare with ambient mantle along an adiabat with $T_a(z) = 1350°C + (0.3\ °C/km)\ z$ (**Figure S3a**).

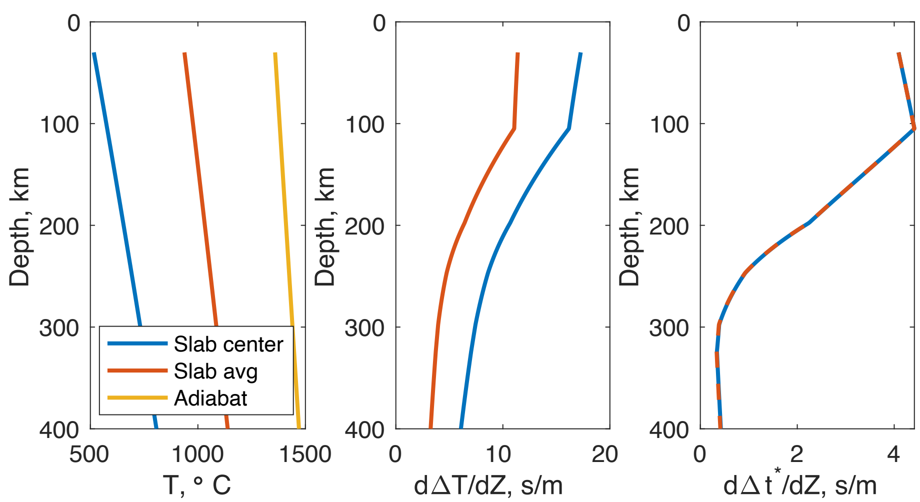

Figure S3. *Model of slab temperature differences between interior and ambient mantle, and resulting velocity or attenuation. (A) Temperatures in slab center, surrounding adiabatic mantle, and average of the two, varying with depth. (B) Resulting velocity differences within slab relative to ambient mantle, expressed as* $d\Delta T/dz$*. For these parameters, the integrated anomaly at the midpoint or maximum is* ΔT *= 2.49 or 4.05 s respectively. (C) resulting attenuation differences within slab relative to ambient mantle, expressed as* $d\Delta t^*/dz$*. For these parameters, the integrated anomaly is* Δt^* *= 0.78 s for both the slab center and midpoint temperature.*

We calculate V_S and $1/Q_S$ using the model of Takei (2017), which includes strong sensitivity near the solidus, embedding the solidus and other elastic parameters in the manner described therein. We estimate density from pressure and temperature assuming a forsterite-90 olivine composition following Abers & Hacker (2016). This results in V_S and Q_S with depth in the ambient mantle and in the slab center. We also track V_S and Q_S at a rough mean temperature for the slab as

$$T_{mid}(z) = \big(T_a(z) + T_{ctr}(z)\big)/2.$$

To estimate the effects on observations, we approximate

$$\left.\frac{d\Delta T_S}{dz}\right|_{ctr} \sim \frac{\Delta z}{V_S(T_a, P)} - \frac{\Delta z}{V_S(T_{ctr}, P)}$$

$$\left.\frac{d\Delta t_S^*}{dz}\right|_{ctr} \sim \frac{\Delta z Q_S^{-1}(T_a, P)}{V_S(T_a, P)} - \frac{\Delta z Q_S^{-1}(T_{ctr}, P)}{V_S(T_{ctr}, P)}$$

and similarly for T_{mid}. These derivatives are shown on **Figure S3**.

The primary conclusion is that temperature variations only affect Δt^* in the upper 150-200 km of the surface, while they affect ΔT at all depths. Second, neither the T_{ctr} nor T_{mid} result in any noticeable attenuation, so the predicted attenuation anomaly is the same for both curves; attenuation is only detectable near the adiabat. This difference between V and Q behavior can explain why the Δt^* measurements only seem to correlate with structure in the upper 150 km, while the ΔT measurements show evidence for slabs much deeper.

Further experiments show that the pattern has little sensitivity to the incoming slab thermal structure, since any temperature < 1000°C produces little attenuation, and the adiabatic mantle is far from the solidus at >50-200 km depth. Changing the potential temperature or the adiabatic gradient affects the depth at which attenuation can be detected, such that hotter mantle shows attenuation anomalies at greater depths. For very young plates (such as Cascadia) the thermal signal of the slab should disappear in V_S at depths of a couple hundred km. Other temperature-attenuation relationships show more subdued effects (e.g., Jackson & Faul, 2010) but generally show shallower sensitivity to Q_S than V_S. In general, attenuation effects are strongest at near-solidus conditions.

Supplementary Text S4. Description of columns in Table S1.

Table S1 lists all station-average measurements in a separate plain-text file. The columns in the table are defined as follows:

STA	Station name
Ntst	Number of stations used in Δt^* estimate; same number for P and S
NdT	Number of stations used in ΔT estimate; same number for P and S
dtstarS	The Δt_S^* estimate
dtstarP	The Δt_P^* estimate

dT_S	The ΔT_S estimate
dT_P	The ΔT_P estimate
sigz_S	The one-sigma uncertainty in Δt_S^*
sigz_P	The one-sigma uncertainty in Δt_P^*
sigT_S	The one-sigma uncertainty in ΔT_S
sigT_P	The one-sigma uncertainty in ΔT_P
Kreg	Region identifier (e.g., Figure 3, inset)

ADDITIONAL REFERENCES

Abers, G.A., and Hacker, B.R., 2016, A MATLAB toolbox and Excel workbook for calculating the densities, seismic wave speeds, and major element composition of minerals and rocks at pressure and temperature: Geochem. Geophys. Geosys. (G3), v. 17, doi:10.1002/2015GC006171.

McKenzie, D.P., 1969, Speculations on the consequences and causes of plate motions: Geophys. J. R. astr. Soc., v. 18, p. 1–32.

Turcotte, D.L., and Schubert, G., 2002, Geodynamics, 2nd Ed.: Cambridge Univ. Press, New York, 456 p.